

Copyright Warning & Restrictions

The copyright law of the United States (Title 17, United States Code) governs the making of photocopies or other reproductions of copyrighted material.

Under certain conditions specified in the law, libraries and archives are authorized to furnish a photocopy or other reproduction. One of these specified conditions is that the photocopy or reproduction is not to be “used for any purpose other than private study, scholarship, or research.” If a user makes a request for, or later uses, a photocopy or reproduction for purposes in excess of “fair use” that user may be liable for copyright infringement,

This institution reserves the right to refuse to accept a copying order if, in its judgment, fulfillment of the order would involve violation of copyright law.

Please Note: The author retains the copyright while the New Jersey Institute of Technology reserves the right to distribute this thesis or dissertation

Printing note: If you do not wish to print this page, then select “Pages from: first page # to: last page #” on the print dialog screen

The Van Houten library has removed some of the personal information and all signatures from the approval page and biographical sketches of theses and dissertations in order to protect the identity of NJIT graduates and faculty.

ABSTRACT

ANALYSIS OF CALIBRATION, ROBUSTNESS, DETECTION OF SPACE-TIME ADAPTIVE RADAR USING EXPERIMENTAL DATA

by
Murat O. Berin

Signal cancellation effects in adaptive array radar are studied under non ideal conditions when there is a mismatch between the true desired signal and the presumed theoretical desired signal. This mismatch results in decreased performance when the estimated correlation matrix has a large desired signal component. The performance of the sample matrix inversion (SMI) method is compared to the eigenanalysis-based eigencanceller method. Both analytical results and the processing on the experimental data from the Mountaintop Program, show that eigenanalysis-based adaptive beamformers have greater robustness to signal cancellation effects than the SMI method. Also, the calibration of the recorded data, and the pulse compression method utilized to achieve high resolution are discussed.

ANALYSIS OF CALIBRATION, ROBUSTNESS, DETECTION OF
SPACE-TIME ADAPTIVE RADAR USING EXPERIMENTAL DATA

by
Murat O. Berin

A Thesis
Submitted to the Faculty of
New Jersey Institute of Technology
in Partial Fulfillment of the Requirements for the Degree of
Master of Science in Electrical Engineering

Department of Electrical and Computer Engineering

January 1996

APPROVAL PAGE

ANALYSIS OF CALIBRATION, ROBUSTNESS, DETECTION OF
SPACE-TIME ADAPTIVE RADAR USING EXPERIMENTAL DATA

Murat O. Berin

Dr. Alexander M. Haimovich, Thesis Advisor Date
Associate Professor of Electrical and Computer Engineering, NJIT

Dr. Yeheskel Bar-Ness, Committee Member Date
Distinguished Professor of Electrical and Computer Engineering
and Director of Center for Communications and Signal Processing, NJIT

Dr. Ali N. Akansu, Committee Member Date
Associate Professor of Electrical and Computer Engineering, NJIT

BIOGRAPHICAL SKETCH

Author: Murat O. Berin
Degree: Master of Science in Electrical Engineering
Date: January 1996
Date of Birth:
Place of Birth:

Undergraduate and Graduate Education:

- Master of Science in Electrical Engineering,
New Jersey Institute of Technology, Newark, NJ, 1996
- Bachelor of Science in Electrical Engineering,
New Jersey Institute of Technology, Newark, NJ, 1994

Major: Electrical Engineering

Awards:

Second Elisha Yegal Bar-Ness Scholarship Award, December 6, 1995

Presentations and Publications:

A. M. Haimovich and M. O. Berin

“Eigenanalysis-Based Space-Time Adaptive Radar: Performance Analysis,”
submitted to *IEEE Trans. Aerospace and Electronics Systems.*, 1995.

A. M. Haimovich and M. O. Berin

“Performance of the Eigencanceler: Eigenanalysis Space-Time Adaptive Radar,” a presentation given at the Adaptive Sensor Array Processing Workshop, March 15-17, 1995, vol. I, p. 419-445.

M. O. Berin A. M. Haimovich

“Signal Cancellation Effects in Adaptive Radar Mountaintop Data-Set ”
in *Proceedings IEEE Int. Conference Acoustics, Speech and Signal Processing*
Atlanta, GA, May 1996.

In memory of my mother
Takuhi Sultan Berin

ACKNOWLEDGMENT

First of all, I would like to thank the committee members. I would like to thank Dr. Bar-Ness, director of the Center for Communications and Signal Processing Research, for his endless efforts to improve the conditions in our lab. It is a tough job, but somebody has to do it. I would like to thank Dr. Akansu for the signal processing theory I learned in his courses. And I would like to thank Dr. Haimovich for being a great advisor. I've gained a lot of theoretical knowledge from him, but most importantly, I learned how to focus on a problem and solve it in an organized fashion, a skill I will appreciate for the rest of my life.

I would like to thank my family, especially my father Sefer, and my sisters Ojen and Yegsabet, for their support and understanding. I do not think I would have been able to accomplish much without their support.

I would like to thank Michael Meyer for his help with Matlab and UNIX in the early stages of this work. I would like to thank Mehmet Tazebay for being a great friend, and his willingness to help with any problem. I would like to thank Lisa Fitton, for checking the grammar of this work and the little talks we had about non-technical issues, which let me get away from the equations and the computers a few minutes a day. I would like to thank Chris Peckham for his help with the \LaTeX style file used to put this work together. I would also like to thank all my friends in the lab for the great discussions on my work or on their work. I must admit, I learned much more by discussing with them than by reading books or papers. Thank you Al Futernik, Jeff Cutcher, Nadir Sezgin, Muzaffer Kanaan, Nahid Kabir, Ashwini Borkar and Shahid Rana.

Last but not least, I would like to thank Murat Okyar, a true friend and a great person, for the fruitful discussions about social issues, politics and life. During my studies for the Master of Science, I have spent a lot of time trying to figure out what I would like to do with my life, and it was a great pleasure meeting Murat

and discussing questions about life with him. Even though I can not say I have the ultimate answer for the meaning of life, he has helped me shape my views and come to conclusions on a few things. Page

I would like to end this acknowledgment with a poem. I just want to remind everyone that we should be a little more careful about what technology brings us. Unfortunately, we make a very big deal out of the improvements in technology and fail to notice the little things in life.

Fueled¹

Fueled
by a million
man-made
wings of fire—
the rocket tore a tunnel
through the sky—
and everybody cheered.
Fueled
only by a thought from God—
the seedling
urged its way
through the thicknesses of black—
and as it pierced
the heavy ceiling of the soil—
and launched itself
up into outer space—
no
one
even
clapped.

Marcie Hans

¹from *Serve Me a Slice of Moon*, by Marcie Hans (Harcourt Bruce Jovanovich, 1965).

TABLE OF CONTENTS

Chapter	Page
1 INTRODUCTION	1
1.1 Signal Model	4
1.2 Joint-Domain and Cascade Processors	7
1.3 Array Improvement Factor	9
2 THE MOUNTAINTOP DATA PACKAGE	12
2.1 Description of the Assets	12
2.2 Calibration	14
2.2.1 Design of Receiver Calibration Filters	14
2.2.2 Design of Antenna Calibration Filters	16
2.3 Pulse Compression	17
3 ROBUSTNESS OF BEAMFORMING ALGORITHMS	22
3.1 Eigenstructure of the Correlation Matrix	23
3.2 Non Adaptive Beamformer	26
3.3 Sample Matrix Inversion	26
3.4 Eigencanceler	27
3.5 Array Improvement Factor Calculations	27
4 MOUNTAIN-TOP DATA ANALYSIS	38
4.1 Description of the Data Files	38
4.2 Target Range Detection	39
4.3 Antenna Pattern	48
4.4 Target Angle Detection	51
4.5 Signal Cancellation	51
4.6 Conclusions	57
APPENDIX A EIGEN-DECOMPOSITION OF A RANK TWO MATRIX	59

TABLE OF CONTENTS
(continued)

Chapter	Page
REFERENCES	61

LIST OF FIGURES

Figure	Page
1.1 Signal Model	5
1.2 Block Diagram of Joint-Domain and Cascade Processors	8
2.1 The Radar Surveillance Technology Experimental Radar (RSTER)	13
2.2 Transversal Linear Prediction Filter	15
2.3 Results of Receiver and Antenna Calibration	18
2.4 Chirp Signal	20
2.5 Chirp Signal Matched Filter Output	21
3.1 Training Regions of the Correlation Matrix	24
3.2 Effects of Desired Signal Component and Pointing Error on the AIF	33
3.3 Effects of Phase Errors and Pointing Error on the AIF	34
3.4 Effects of Amplitude Errors and Pointing Error on the AIF	35
3.5 Effects of Signal-to-Noise Ratio and Pointing Error on the AIF	36
3.6 Effects of Desired Signal Angle and Pointing Error on the AIF	37
4.1 Magnitude Plot of Range Returns on IDPCA Data, CPI 6, PRI 1	40
4.2 Doppler-Azimuth Plot for Target Range Cell	40
4.3 Eigenvalues of the Data	41
4.4 Joint-Domain Range Plots Using 300 Training Points	44
4.5 Post-Doppler Range Plots Using 300 Training Points	45
4.6 Post-Doppler Range Plots Using 50 Training Points	46
4.7 Post-Doppler Range Plots Using 28 Training Points	47
4.8 Post-Doppler Antenna Pattern Plots Using 300 Training Points	49
4.9 Post-Doppler Antenna Pattern Plots Using 50 Training Points	50
4.10 Post-Doppler Antenna Pattern Plots Using 28 Training Points	52
4.11 Post-Doppler Target Detection Using 300 Training Points	53

LIST OF FIGURES
(continued)

Figure	Page
4.12 Post-Doppler Target Detection Using 50 Training Points	54
4.13 Post-Doppler Target Detection Using 28 Training Points	55
4.14 Signal Cancellation	58

CHAPTER 1

INTRODUCTION

Adaptive antennas have been under development in various forms for about three decades. Examples of adaptive arrays and their applications are the Howells-Applebaum sidelobe canceler [1], Widrow's [2], Griffith's [3] Frost's [4], Zahm's [5] Compton's beamformer [6]. Frost has shown that under ideal conditions, linearly constrained array beamforming provides an improvement in array output signal-to-interference-plus-noise ratio (SNIR) in comparison to conventional beamforming. Conventional beamformers cancel the interference without considering a desired signal. A linearly constrained adaptive array, however, tries to preserve signals at a given angle and/or Doppler frequency. To preserve a presumed desired signal, a steering vector is formed using theoretical output of the antenna array under ideal conditions. This steering vector is used to calculate the weights for a given adaptive criteria, such that there is some gain in the *direction* of the desired signal. However, due to practical limitations the presumed steering vector and the true desired signal do not necessarily match. This mismatch, also known as the perturbation problem, causes signal cancellation when the optimum array processor is used.

The perturbation problem, which has many sources, has been an active research topic. The perturbation due to pointing errors, mismatch between the presumed and true angle of arrival, was studied by Er [7]. Using hybrid techniques were suggested to overcome pointing errors by Habu [8]. Another source of mismatch is the calibration errors that results in random gain and phase errors at every element. The gain and phase mismatches are caused by unmatched antennas and receiver electronics, producing a different response at every channel. Previous work on calibration effects includes the problem of small phase errors at each element [9], and the more general case of amplitude and phase errors [10, 11, 12]. Certain array processing criteria

also requires a prior knowledge of the interference correlation matrix, i.e. the Wiener solution. In general, the true correlation matrix of the interference and noise is not available and it needs to be estimated from a finite record of the data. The estimation error, due to training set size limitation, affects the performance of the array. Using a larger training set for a better estimate, may also result in problems if the data is not completely stationary. If the training data set includes the desired signal, the estimated correlation matrix has a desired signal component. If the desired signal component is large, the processor interprets the desired signal portion mismatched to the steering vector as interference, and signal suppression is observed even with a small steering vector perturbation [13, 14].

The sample matrix inversion (SMI) method was pioneered by Brennan and Reed [15, 16]. They proposed to use a signal free secondary data set to estimate the interference correlation matrix, and to utilize the Wiener solution to optimize the weights. If the data is not homogeneous, training in a different region causes a large estimation error resulting decreased performance. The other alternative, retraining the processor anew for each range cell under test such that the cell is excluded from the training set, adds considerable computational complexity. The performance of the SMI is also degraded if the estimation is performed around the target region due to the residual power of the target signal resulting in a correlation matrix with a large desired signal component. Recently, eigenanalysis based beamformers have been considered for adaptive array space time radar. Haimovich suggests an eigenanalysis interference canceler and shows the superior performance of the eigenanalysis techniques when data length used for training is relatively short [17]. The principal component inverse (PCI) method was suggested by Kirsteins [18] One approach to eigenanalysis based beamforming is the two step adaptive interference nulling algorithm by Marshall [19]. In two step nulling, the data is transformed to a lower dimension using the signal-plus-interference eigenvectors, and the optimum

processing is carried in the transform domain. This approach overcomes the low rank problem of the correlation matrix, observed when the training set is small. Transform method can be also implemented by using the projection of the steering vector onto the signal-plus-interference subspace [20]. A sub optimum approach is the eigencanceler, formulated as a modified minimum variance beamformer [21]. The eigencanceler constrains the weight vector in the noise subspace and nulls the interference subspace. The desired signal power in the interference subspace is lost due to the subspace nulling, but the performance of the eigencanceler, which is less complex, is very close to the transform method. Eigenanalysis based processing also can be carried out by using the projection of the optimal weight vector on the signal-plus-interference subspace [22]. All eigenanalysis based beamformers have better convergence rate than the SMI in terms of the training support required to achieve specified performance. Eigenanalysis based beamformers are also robust against steering vector perturbation. In this work, the SMI method and the eigencanceler are compared analytically, and the analytical results are verified on the Mountaintop data package.

Others who have made important contributions to analysis of the mismatch problem include Widrow [23], Bar-Ness [24], Jablon [25].

In the remaining part of this chapter, the signal model, and the adaptive space time processors are discussed, and the array improvement factor is defined. In chapter 2, the Mountaintop program is described, and the calibration filter design and the pulse compression are discussed. In chapter 3, the performance of two adaptive algorithms, SMI and the eigencanceler, are studied analytically. And in chapter 4, the analytical results are verified using the experimental data from the Mountaintop data package.

1.1 Signal Model

Consider a narrow-band antenna array consisting of N omni-directional sensors in a linear spatial configuration. A coherent pulse is transmitted and the returns from the range cells are recorded from t_{start} to t_{end} seconds after the transmission. The time interval from the start of one transmitted pulse to the start of the next pulse is called the pulse repetition interval (PRI). K coherent PRI's form a coherent pulse interval (CPI). To analyze a specific range cell at distance r_d , snapshot row vectors at t_d seconds from the start of each PRI are stacked to form the data matrix \mathbf{X} . The relationship between r_d and t_d is given by

$$r_d = \frac{t_d c}{2}, \quad (1.1)$$

where c is the speed of light and the data matrix \mathbf{X} is given by

$$\mathbf{X} = \begin{bmatrix} x_{1,1} & x_{1,2} & \cdots & x_{1,N} \\ x_{2,1} & x_{2,2} & \cdots & x_{2,N} \\ \vdots & \vdots & \ddots & \vdots \\ x_{K,1} & x_{K,2} & \cdots & x_{K,N} \end{bmatrix}. \quad (1.2)$$

where $x_{k,n}$ is the complex envelope of the echo signal at the k^{th} PRI and the n^{th} antenna. If a target is present at a given range cell, \mathbf{X} has the form

$$\mathbf{X} = \mathbf{X}_d + \mathbf{X}_i + \mathbf{X}_n, \quad (1.3)$$

where \mathbf{X}_d is the target signal (desired signal), \mathbf{X}_i is the interference, and \mathbf{X}_n is the noise matrix. If a target is not present in a given range cell then

$$\mathbf{X} = \mathbf{X}_i + \mathbf{X}_n. \quad (1.4)$$

The columns of \mathbf{X}_d are samples in time that give information about the velocity of the target. The rows of this matrix are samples in space that give information about the angle of the received signal. To study how these quantities relate to the measurements, consider a plane wave, as shown in Figure 1.1. In the ideal case, when

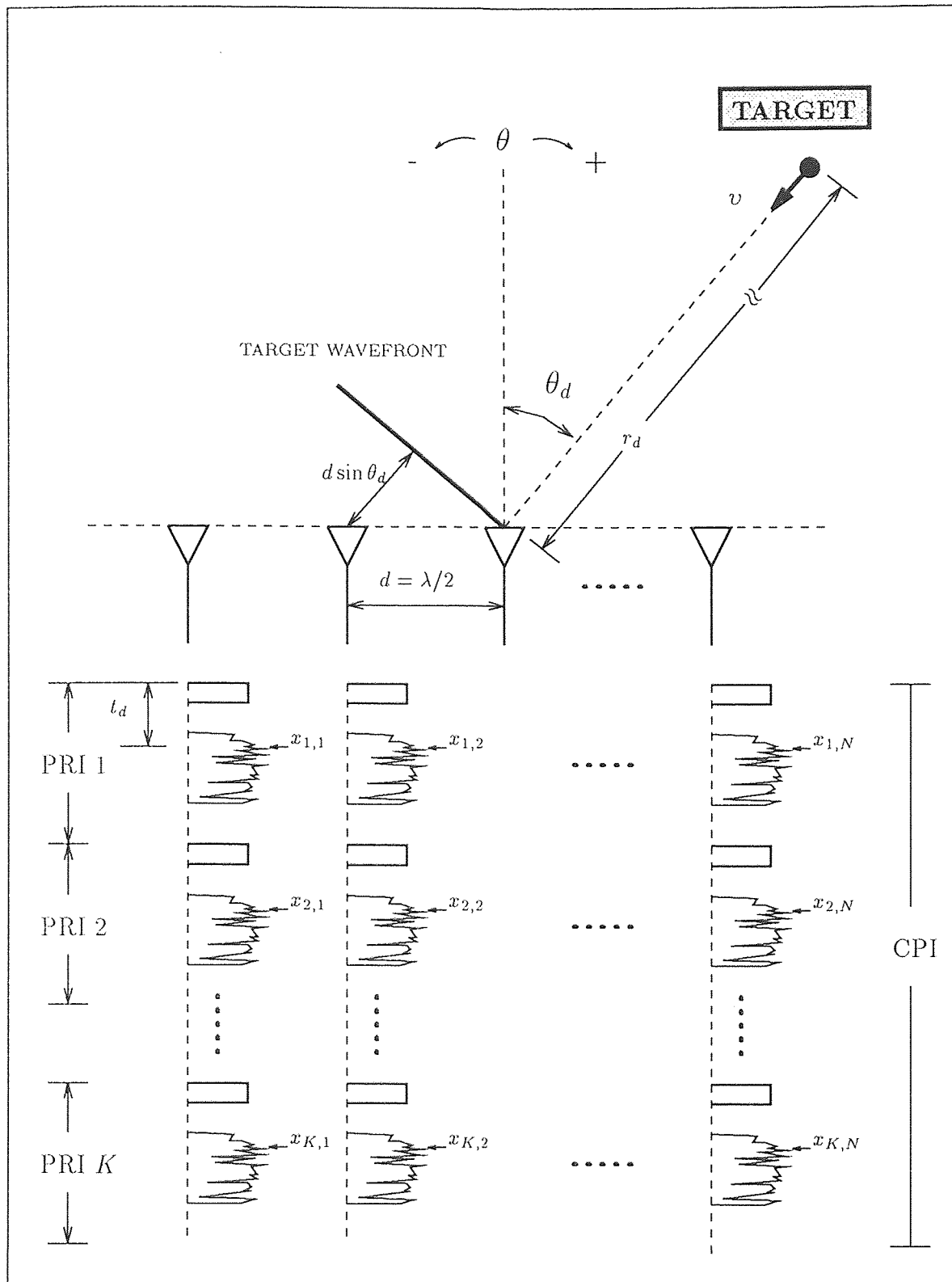


Figure 1.1 Signal Model

the spatial channels are co-linear, identical, omni-directional and equally spaced with spacing d , the entries of matrix \mathbf{X}_d are given by

$$x_d(k, n) = \frac{\sigma_d}{\sqrt{KN}} e^{j2\pi((k-1)\psi_t + (n-1)\psi_s)}, \quad (1.5)$$

where σ_d^2 is the desired signal power, ψ_s is the normalized spatial frequency and ψ_t is the normalized Doppler frequency. The normalized spatial frequency is given by

$$\psi_s = \frac{d \sin \theta_d}{\lambda}, \quad (1.6)$$

where λ is the wavelength of the transmitted signal and θ_d is angle of the target. The normalized Doppler frequency is given by

$$\psi_t = \frac{2vPRI}{\lambda}, \quad (1.7)$$

where v is the radial velocity of the target. The desired signal component of the matrix \mathbf{X} , under ideal conditions, can also be written as

$$\mathbf{X}_d = \sigma_d \mathbf{s}_t \mathbf{s}_s^T, \quad (1.8)$$

where \mathbf{s}_t , the $K \times 1$ normalized temporal steering vector, and \mathbf{s}_s , the $N \times 1$ normalized spatial steering vector, are given by

$$\mathbf{s}_t = \frac{1}{\sqrt{K}} \begin{bmatrix} 1 \\ e^{j2\pi\psi_t} \\ \vdots \\ e^{j2\pi(K-1)\psi_t} \end{bmatrix} \quad \text{and} \quad \mathbf{s}_s = \frac{1}{\sqrt{N}} \begin{bmatrix} 1 \\ e^{j2\pi\psi_s} \\ \vdots \\ e^{j2\pi(N-1)\psi_s} \end{bmatrix}. \quad (1.9)$$

The $KN \times 1$ normalized joint-domain steering vector is formed by stacking the transpose of the rows of \mathbf{X}_d and it is given by

$$\mathbf{s}_j = \mathbf{s}_t \otimes \mathbf{s}_s, \quad (1.10)$$

where \otimes is the Kronecker product. Assuming PRI , d , and λ have been properly chosen to meet the Nyquist sampling criterion, ψ_s and ψ_t are confined within $[-0.5, 0.5]$.

1.2 Joint-Domain and Cascade Processors

For space-time radar, joint-domain and cascade processing are two possible configurations. With the joint-domain linear processor (see Figure 1.2(a)), the data is processed as follows,

$$\eta_j = \mathbf{w}_j^H \mathbf{x}_j, \quad (1.11)$$

where \mathbf{w}_j is the $KN \times 1$ joint domain weight vector and \mathbf{x}_j is the $KN \times 1$ joint-domain data vector formed by stacking the transpose of the rows of the data matrix \mathbf{X} :

$$\mathbf{x}_j = \begin{bmatrix} x_{1,1} \\ \vdots \\ x_{1,N} \\ x_{2,1} \\ \vdots \\ x_{2,N} \\ \vdots \\ x_{K,1} \\ \vdots \\ x_{K,N} \end{bmatrix}. \quad (1.12)$$

There are two cascade configurations: time-space (T-S) and space-time (S-T). The T-S configuration consists of K -dimensional temporal processing followed by N -dimensional spatial processing. S-T configuration processes the data in the opposite order. Block diagrams of cascade configurations are shown in Figure 1.2 (b) and (c). In the T-S configuration the input to the temporal processing stage is data matrix \mathbf{X} . The output of this stage is the $N \times 1$ spatial data vector:

$$\mathbf{x}_s = \mathbf{X}^T \mathbf{w}_t^*, \quad (1.13)$$

where \mathbf{w}_t is the $K \times 1$ temporal weight vector and (*) means complex conjugate. The output of the temporal processor is used by the spatial processor, which produces

$$\eta_{ts} = \mathbf{w}_s^H \mathbf{x}_s, \quad (1.14)$$

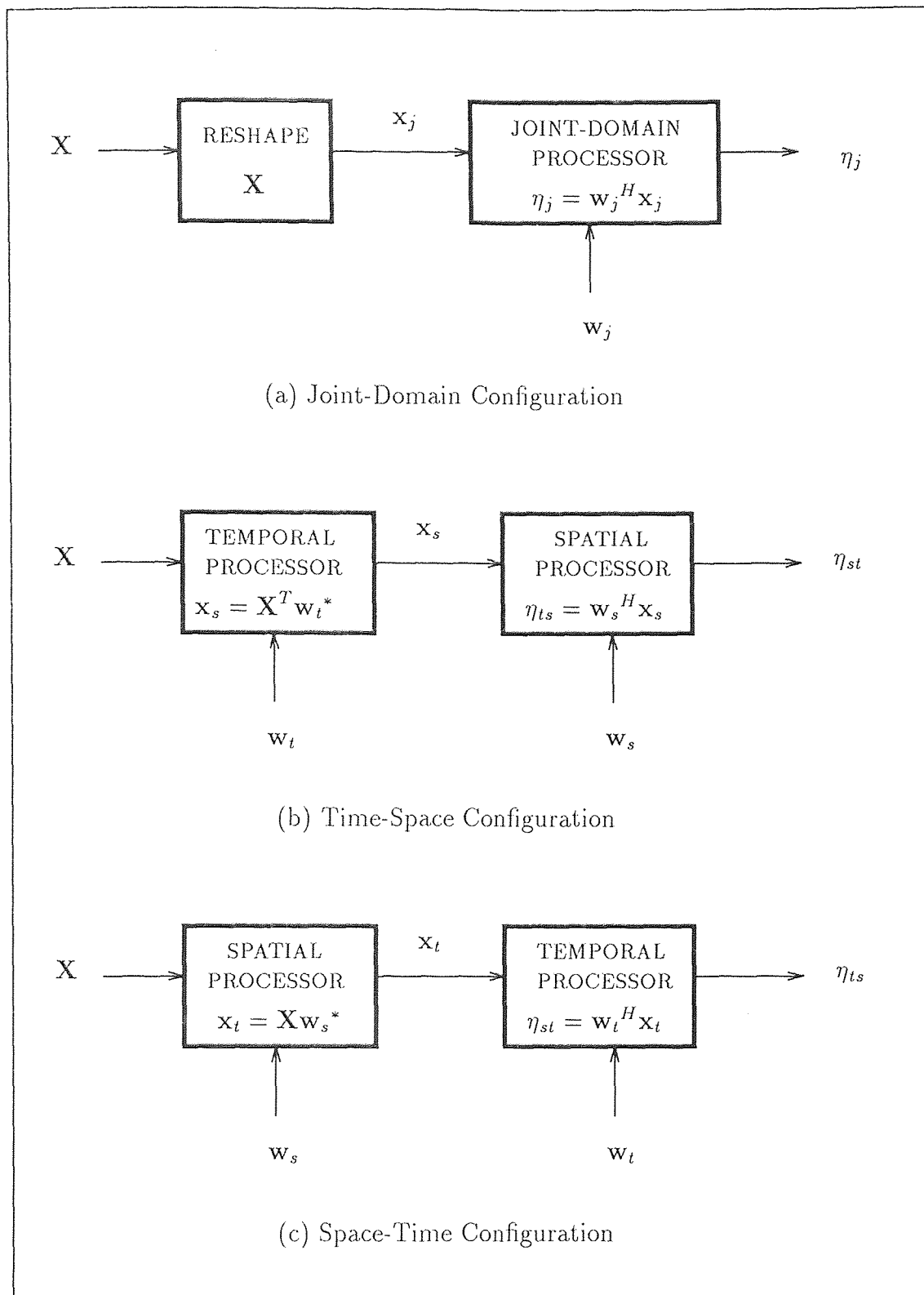


Figure 1.2 Block Diagram of Joint-Domain and Cascade Processors

where \mathbf{w}_s is an $N \times 1$ spatial weight vector. Similarly, for the S-T configuration the output of the spatial beamformer is

$$\mathbf{x}_t = \mathbf{X}\mathbf{w}_s^*, \quad (1.15)$$

where \mathbf{x}_t is the $K \times 1$ temporal data vector and the output of the temporal beamformer is

$$\eta_{st} = \mathbf{w}_t^H \mathbf{x}_t. \quad (1.16)$$

Both of these cascade configurations may use different adaptive criteria for processing in both domains. The performance of the cascade should approach that of the optimum processor with the same configuration. Cascade processing, especially the S-T configuration, has been very popular in recent years, but it has been shown that joint-domain processing performs better than both cascade configurations [26].

In chapter 4, the joint-domain and the post-Doppler processors are applied to the Mountaintop data. The post-Doppler processor has a cascade configuration with a non-adaptive temporal processor followed by an adaptive spatial processor. Next, the figure of merit used in this work to compare the performance of the adaptive algorithms is discussed

1.3 Array Improvement Factor

Under the assumption of uncorrelated signal, interference and noise, the correlation matrix of the data vector \mathbf{x} , which may have the form of \mathbf{x}_j , \mathbf{x}_t or \mathbf{x}_s , is given by

$$\mathbf{R}_x = E[\mathbf{x}\mathbf{x}^H] = \sigma_d \mathbf{R}_d + \sigma_i^2 \mathbf{R}_i + (\sigma_n^2/L)\mathbf{I}, \quad (1.17)$$

where L is the length of the data vector \mathbf{x} , σ_d^2 is the desired signal power and \mathbf{R}_d is the autocorrelation of the desired signal given by

$$\mathbf{R}_d = \mathbf{x}_d \mathbf{x}_d^H. \quad (1.18)$$

Under the ideal conditions, the desired signal vector \mathbf{x}_d has the form of equation (1.9) or equation (1.10), depending on the configuration of the beamformer. \mathbf{R}_i is the autocorrelation of the interference, σ_i^2 is the interference power, and σ_n^2 is the power of the white Gaussian noise. \mathbf{R}_d and \mathbf{R}_i are normalized to have a trace of one.

The output power of the beamformer as a function of \mathbf{w} is given by

$$\begin{aligned} P_{BF}(\mathbf{w}) &= E \left[|\mathbf{w}^H \mathbf{x}|^2 \right] = E \left[\mathbf{w}^H \mathbf{x} \mathbf{x}^H \mathbf{w} \right] \\ &= \mathbf{w}^H \mathbf{R}_x \mathbf{w} \\ &= \sigma_d^2 \mathbf{w}^H \mathbf{R}_d \mathbf{w} + \sigma_i^2 \mathbf{w}^H \mathbf{R}_i \mathbf{w} + (\sigma_n^2/L) \mathbf{w}^H \mathbf{w}. \end{aligned} \quad (1.19)$$

The first term of P_{BF} is the signal power and the remaining is the interference-plus-noise power. Signal-to-interference-plus-noise ratio at the output of the beamformer is given by

$$SNIR_{BF} = \frac{\sigma_d^2 |\mathbf{w}^H \mathbf{x}_d|^2}{\sigma_i^2 \mathbf{w}^H \mathbf{R}_i \mathbf{w} + (\sigma_n^2/L) \mathbf{w}^H \mathbf{w}} = \frac{SNR |\mathbf{w}^H \mathbf{x}_d|^2}{INR \mathbf{w}^H \mathbf{R}_i \mathbf{w} + (1/L) \mathbf{w}^H \mathbf{w}}, \quad (1.20)$$

where $SNR = \sigma_d^2/\sigma_n^2$ and $INR = \sigma_i^2/\sigma_n^2$.

The array improvement factor (AIF) is defined as the ratio of $SNIR_{BF}$ to SNR at the input of the beamformer as a function of the weight vector:

$$G(\mathbf{w}) = \frac{|\mathbf{w}^H \mathbf{x}_d|^2}{\mathbf{w}^H \mathbf{R}_{i+n} \mathbf{w}}, \quad (1.21)$$

where \mathbf{R}_{i+n} is the interference-plus-noise correlation matrix defined as

$$\mathbf{R}_{i+n} = INR \mathbf{R}_i + (1/L) \mathbf{I}. \quad (1.22)$$

Assuming \mathbf{x}_d and \mathbf{R}_{i+n} are known, $SNIR_{BF}$ is maximized by the Wiener solution given by

$$\mathbf{w}_o = k \mathbf{R}_{i+n}^{-1} \mathbf{x}_d \quad \text{and} \quad G(\mathbf{w}_o) = \mathbf{x}_d^H \mathbf{R}_{i+n}^{-1} \mathbf{x}_d, \quad (1.23)$$

where k is a gain constant and does not have an effect on the AIF. To study the behavior of the AIF, first consider a noise only correlation matrix ($\sigma_i^2 = 0$), For this

case the weight vector and the AIF are given by

$$\mathbf{w}_o = k\mathbf{x}_d \quad \text{and} \quad G_n(\mathbf{w}_o) = L. \quad (1.24)$$

With a single interferer ($\mathbf{R}_i = \mathbf{x}_i\mathbf{x}_i^H$), inverse of the correlation matrix is given by

$$\mathbf{R}_{i+n}^{-1} = (INR\mathbf{x}_i\mathbf{x}_i^H + (1/L)\mathbf{I})^{-1} = L\mathbf{I} - \frac{INR \cdot L}{1 + INR \cdot L}\mathbf{x}_i\mathbf{x}_i^H, \quad (1.25)$$

and the AIF is given by

$$G_{i+n}(\mathbf{w}_o) = L - \frac{INR \cdot L}{1 + INR \cdot L} |\mathbf{x}_d^H \mathbf{x}_i|^2. \quad (1.26)$$

G_{i+n} is confined within $[(L-1), L]$; the maximum value is achieved when the $INR = 0$ or $\mathbf{x}_d^H \mathbf{x}_i = 0$ and the lower limit is obtained when the $INR = \infty$ and $\mathbf{x}_d^H \mathbf{x}_i = 1$.

However, in many cases of practical importance the available information about the desired signal vector is imprecise. Also, the correlation matrix of interference-plus-noise is estimated using a finite set of data. These two practical problems cause a decrease in performance of the Wiener solution. In chapter 3, the AIF will be used as the figure of merit to compare the performance of the SMI and the eigencanceler methods under these conditions.

CHAPTER 2

THE MOUNTAINTOP DATA PACKAGE

The Mountaintop Program was initiated to study advanced processing techniques and technologies required to support the mission requirements of the next generation airborne early warning platform. In this chapter, the radar and the data processing aspects such as calibration and pulse compression are discussed.

2.1 Description of the Assets

Two major assets of the Mountaintop Program are Radar Surveillance Technology Experimental Radar (RSTER) and Inverse Display Phase Central Array (IDPCA). RSTER is a 5 meter by 10 meter vertically polarized array made up of 14 row elements with an independent phase shifter, transmitter and receiver. This original configuration, with adaptivity in elevation, is referred to as the RSTER configuration. The antenna was designed to be mounted vertically to achieve azimuth adaptivity. This configuration is referred to as RSTER-90. The basic set up of the data collection is given in Figure 2.1. IDPCA was developed to overcome the challenge of providing a meaningful emulation of the airborne surveillance environment. For a fixed radar, IDPCA produces clutter returns with the same spatial and temporal characteristics as observed from an airborne surveillance platform. Since clutter profile in azimuth-Doppler space is due to the motion of the aperture's phase center, to effect the emulation one can move an antenna or deploy several antennas and move between them. Apparent motion occurs along the length of the array. The IDPCA is a transmit-only device and the clutter returns are received through the larger RSTER-90 antenna. The effectiveness of the IDPCA's motion was demonstrated by comparing the clutters returns of IDPCA to clutter returns using a Lear jet [27].

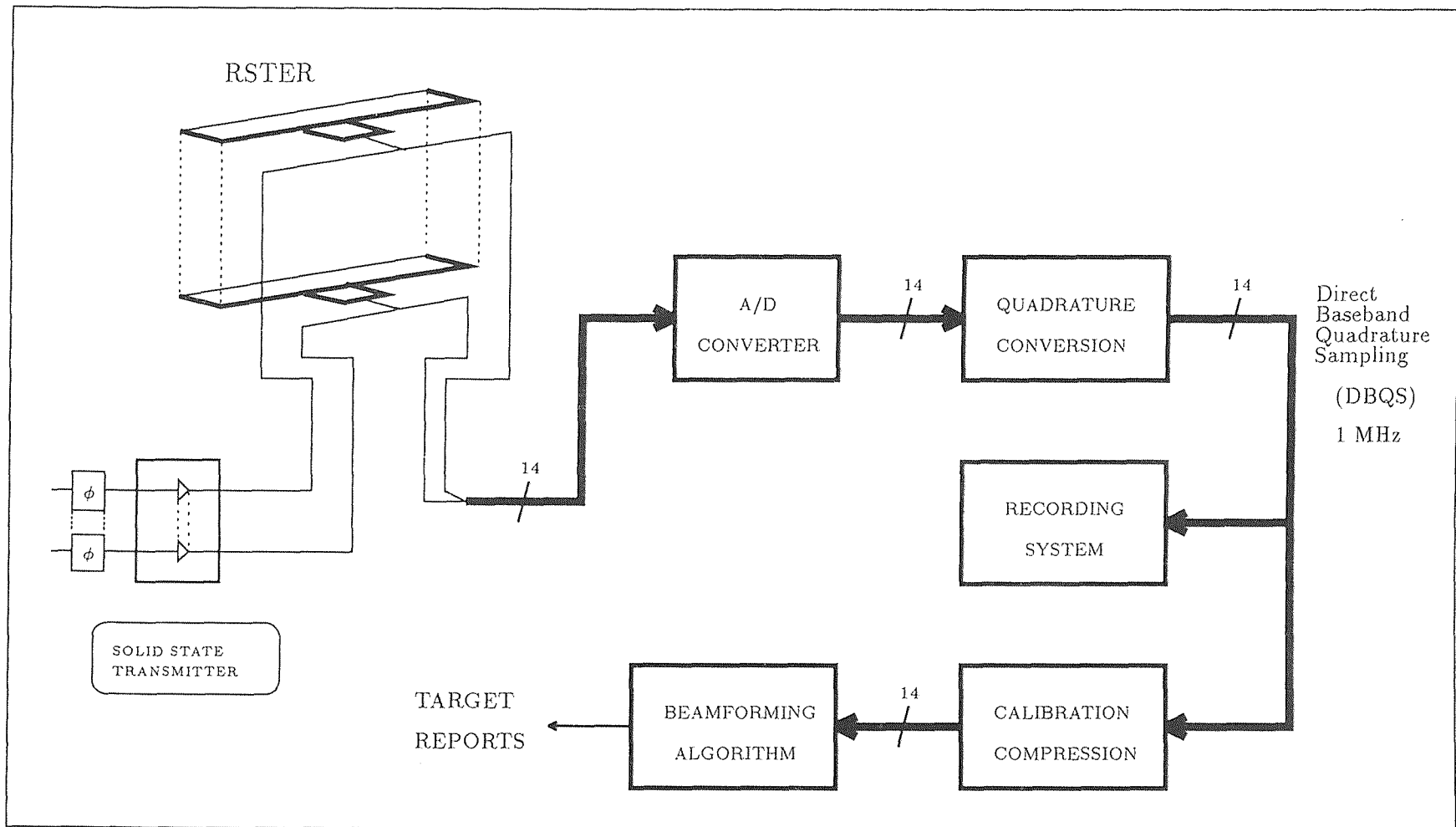


Figure 2.1 The Radar Surveillance Technology Experimental Radar (RSTER)

2.2 Calibration

Theory of array processing is developed assuming ideal elements (channels) with omni-directional, identical and equally spaced antennas and perfectly matched channel receiver electronics. However, to satisfy these ideal conditions is an impossible challenge. The hardware calibration is limited by the current available technology, but the calibration can be enhanced by using digital filters to compensate for the differences in the receiver electronics, and the antenna mismatches. In this section, the design of the digital calibration filters are discussed.

Calibration is done in two stages: Receiver Calibration (RCAL) and Antenna Calibration (ACAL). RCAL covers differences in amplitude and phase ripple between channels at intermediate frequency (IF). ACAL compensates for amplitude and phase match differences between channels at radio frequency (RF). RCAL and ACAL files are recorded while two different, known test signals are injected into antenna/receiver hardware. For RCAL, a 1 MHz LFM is injected into all channels of RSTER in the IF portion of the receiver, after the RF channel equalizer filters. During the injection of this test signal, data is recorded after A/D conversion and direct baseband quadrature sampling (DBQS) at a 1 MHz rate. For ACAL a 500 KHz LFM signal is injected at the antenna immediately after the duplexer assembly. Data is recorded after the A/D, using DBQS at 1 MHz sampling. Complex weights are determined from this data set in order to equalize the channels.

2.2.1 Design of Receiver Calibration Filters

The band limited receiver is modeled with a transfer function. RCAL files are used to design a transversal filter, which estimates the receiver transfer functions and equalizes to match each channel to the reference channel. The output of a transversal filter, as shown in Figure 2.2 is given by the finite convolution sum

$$y_i(n) = \sum_{k=0}^{M-1} w_k^* u_i(n-k), \quad (2.1)$$

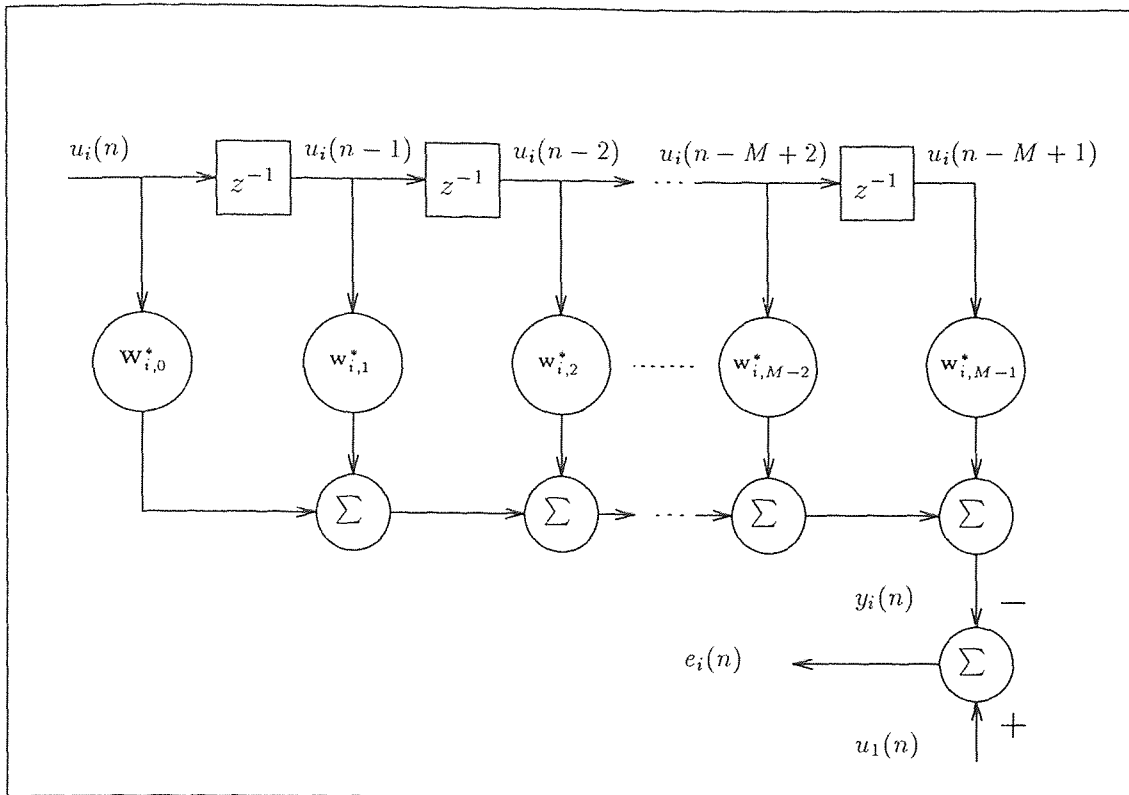


Figure 2.2 Transversal Linear Prediction Filter

where M denotes the number of taps, $u(n)$ is the input to the filter and w_k are the weights calculated using the least squares (LS) algorithm. The output of the first antenna, $u_1(n)$, is used as the reference signal. To calculate the weights for the i^{th} element, the LS algorithm minimizes the power of the error function given by

$$e_i(n) = u_1(n) - \sum_{k=0}^{M-1} w_{i,k}^* u_i(n-k). \quad (2.2)$$

Assuming N samples of data are recorded, it can be easily shown [28][29] that the error function, $e_i(n)$, is minimized when

$$\mathbf{w}_i = \mathbf{A}^+ \mathbf{u}_1, \quad (2.3)$$

where

$$\mathbf{w}_i = \begin{bmatrix} w_{i,0} \\ w_{i,1} \\ \vdots \\ w_{i,M-1} \end{bmatrix}, \quad \mathbf{u}_1 = \begin{bmatrix} u_1^*(M-1) \\ u_1^*(M) \\ \vdots \\ u_1^*(N-1) \end{bmatrix}, \quad (2.4)$$

$$\mathbf{A}^H = \begin{bmatrix} u_i(M-1) & u_i(M) & \cdots & u_i(N-1) \\ u_i(M-2) & u_i(M-1) & \cdots & u_i(N-2) \\ \vdots & \vdots & \ddots & \vdots \\ u_i(0) & u_i(1) & \cdots & u_i(N-M) \end{bmatrix}, \quad (2.5)$$

and (+) denotes pseudo-inverse for an over determined system given by

$$\mathbf{A}^+ = (\mathbf{A}^H \mathbf{A})^{-1} \mathbf{A}^H. \quad (2.6)$$

2.2.2 Design of Antenna Calibration Filters

The antenna calibration is the second stage of the calibration. Amplitude and phase correction is utilized to overcome mismatches between signals at the receiver inputs. The antenna mismatch is modeled as a single complex weight, since the antenna has a large bandwidth. A known test signal is injected immediately after the duplexer assembly, and the output is recorded at the output of A/D into ACAL files. Since the ACAL signal travels through both the channel front end and the receiver portion, prior to determining the antenna calibration weights, the data is equalized using

RCAL weights. This equalization step is only needed if the injected test signal is LFM, and not needed if it is a single frequency. To calculate the single weight needed for the i_{th} element of the array, equation (2.3) is used with $M = 1$. Again, the output of the first antenna, $u_1(n)$, is used as the reference signal.

Figure 2.3 illustrates the effects of the calibration process. Shown is CPI 1 of ACAL file `acal585v1.mat` before and after calibration. In Figure 2.3(a), the magnitude of channel outputs are plotted on top of each other. Every channel's output has a different shape and amplitude for the same injected test signal. In Figure 2.3(b), the same data is plotted after receiver equalization using RCAL weights designed with the RCAL file `rcal585v1.mat` and $M = 31$. Compared with Figure 2.3(a) the equalized channel outputs have the same shape but different amplitude. The amplitude differences are calibrated using ACAL weights, which are designed using the ACAL file after receiver calibration. In Figure 2.3(c) the output of the channels are plotted after the antenna calibration, where all the outputs have the same shape and amplitude.

2.3 Pulse Compression

In order to receive measurable target returns, the transmitted pulse must have enough energy. A signal with a larger amplitude may be transmitted to increase the energy of the signal but the amplitude of the signal is limited by the transmitter power. An other approach is to use a longer pulse, but this causes problems with the resolution of the radar. For example, if a $100 \mu s$ pulse is transmitted, using equation (1.1), this would result in a 15 km resolution which is not practical. The Mountaintop radar uses pulse compression to achieve high range resolution. The radar transmits a wideband Chirp pulse. The chirp radar concept is described in detail by Klauder [30] and Wehner [14]. Samples of the complex envelope of a chirp signal is given by

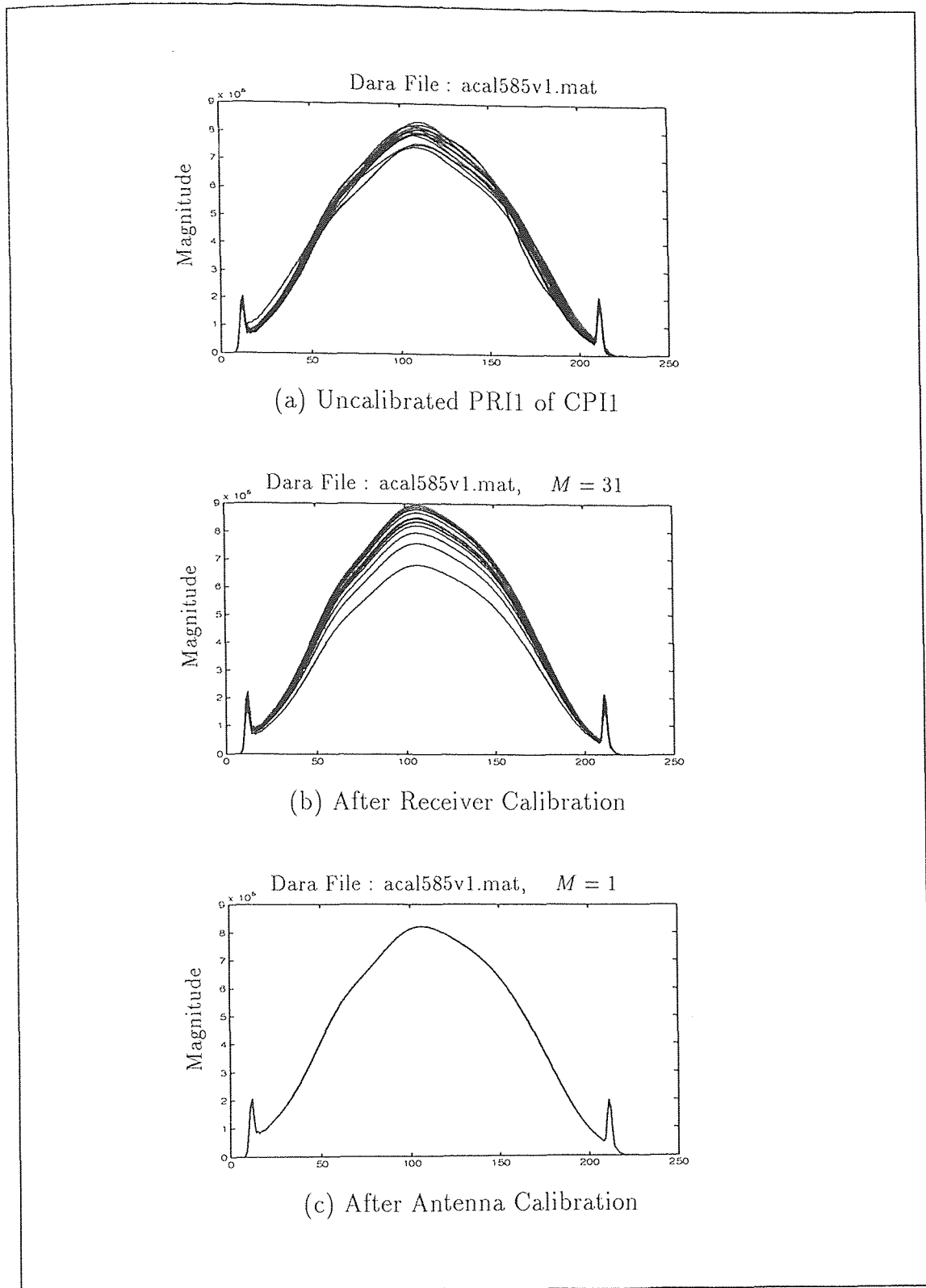


Figure 2.3 Results of Receiver and Antenna Calibration

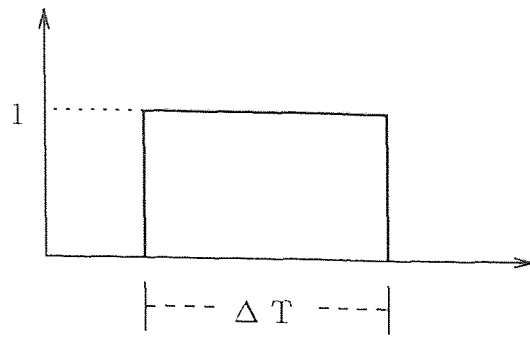
the relation

$$s(n) = e^{j2\pi(wn^2/2-n/2)} \quad n = 0, 1, \dots, N-1, \quad (2.7)$$

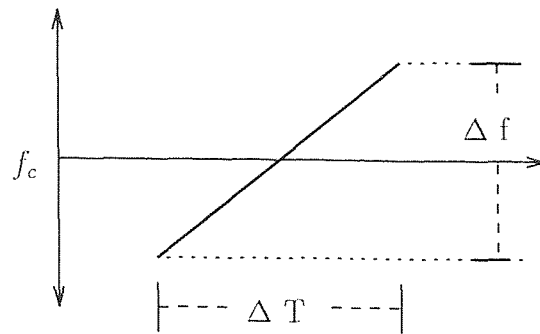
where N is the number of samples taken during the pulse and assuming Nyquist sampling rate, $w = 1/(N-1)$. A plot of the transmitted pulse envelope, pulse frequency, and RF wave form as a function of time, is given in Figure 2.4 (a), (b), and (c), respectively. The matched filter to this pulse is given by

$$s(n) = e^{j2\pi(wn^2/2+n/2)} \quad n = -N+1, -N+2, \dots, 0. \quad (2.8)$$

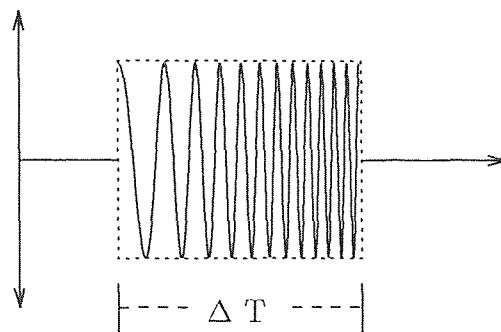
The output of the matched filter is plotted in Figure 2.5. To generate these plots, a $100 \mu s$ pulse is used with a $1 \mu s$ sampling period which results in 100 samples, $N = 100$. Using this method the $100 \mu s$ pulse is compressed to give a resolution of $1 \mu s$ which corresponds to 150 m. The largest sidelobe is 13 dB below the main lobe. Windowing can be used to get lower sidelobes, but this will cause a wider mainlobe. In chapter 4, none of the plots generated using the experimental data used windowing on pulse compression.



(a) Transmitted Pulse Envelope

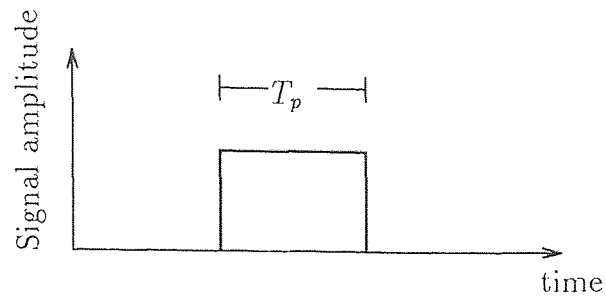


(b) Transmitted Pulse Frequency

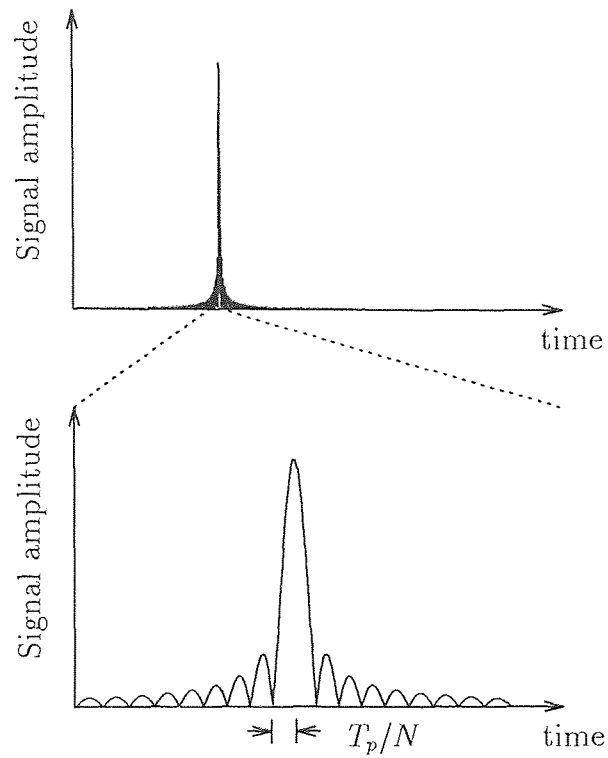


(c) Transmitted Pulse RF Waveform

Figure 2.4 Chirp Signal



(a) Received Pulse Envelope



(b) Output of the Matched Filter

Figure 2.5 Chirp Signal Matched Filter Output

CHAPTER 3

ROBUSTNESS OF BEAMFORMING ALGORITHMS

Linearly constrained array processing outperforms the conventional non-adaptive beamformer in terms of improving the signal-to-interference-plus-noise ratio at the output of the array. However, the performance is degraded by two major effects, the mismatch of the desired signal with the presumed steering vector and the presence of the desired signal in the data used for the estimation of the correlation matrix.

The mismatch effect, also known as the perturbation problem, has two sources. The first is the calibration error, which is due to the antenna mismatch that causes different gain and phase at every element. The second is the pointing error, which is due to the mismatch between the true angle of arrival and the presumed angle of arrival.

Performance degradation due to the desired signal component in the correlation matrix was studied in [13] and [20]. The the Wiener solution, given in equation (1.23), assumes a known correlation matrix of the interference-plus-noise, but there are two practical issues degrade the performance. These are the finite number of data samples used in the estimate and the presence of the desired signal in the training data set.

In this chapter the performance of the SMI and the eigencanceler methods are compared analytically with respect to the steering vector mismatch problem. Both of these methods use the estimated correlation matrix for optimization of the weights, therefore, first the properties of the correlation matrix is discussed. After a small discussion on the two adaptive method, the array improvement factors for the spatial processor are studied. For analytical simplicity, a single desired signal and a single interferer are assumed. Non-adaptive beamformer, which will be used in chapter 4 on the experimental data as the clutter reference, is also discussed briefly.

3.1 Eigenstructure of the Correlation Matrix

The correlation matrix has a very important role in the performance of adaptive algorithms, therefore, in this section the eigen-decomposition and some important properties of the correlation matrix are presented. In practice, the correlation matrix is generally not known and needs to be estimated from the data. Maximum likelihood estimate of the correlation matrix is given by

$$\widehat{\mathbf{R}}_x = \frac{1}{M} \sum_{m=1}^M \mathbf{x}_m \mathbf{x}_m^H, \quad (3.1)$$

where \mathbf{x}_m is an $L \times 1$ data vector and M is the number of data vectors used to estimate the correlation matrix. The larger the data support the better the estimate (training). However if the data is not stationary, this approach may do more harm than good. The adaptive methods utilize the correlation matrix to cancel the interference, therefore a desired signal free correlation matrix is desired in order to prevent signal cancellation. To achieve a desired signal free correlation matrix a secondary data set may be used as shown in Figure 3.1(a). But this approach results in a large estimation error if the data is not stationary. An other method to get a signal free correlation matrix is to utilize a data set around the data vectors of interest with the data vector under test omitted from the training, as seen in Figure 3.1(b). This approach causes additional complexity because for every test data vector a new estimate is calculated. If the training is done as seen in Figure 3.1(c) with the test data vector in the training set, this causes a large desired signal component in the correlation matrix when the target is present, and signal cancellation is observed.

The correlation matrix $\widehat{\mathbf{R}}_x$ can be decomposed into eigenvalues and eigenvectors using the spectral theorem,

$$\widehat{\mathbf{R}}_x = \sum_{l=1}^L \lambda_l \mathbf{q}_l \mathbf{q}_l^H, \quad (3.2)$$

where λ_l and \mathbf{q}_l are the l^{th} eigenvalue and eigenvector, respectively. Eigenvalues are sorted from largest to smallest: $\lambda_1 > \lambda_2 > \dots > \lambda_{L-1} > \lambda_L$. The inverse of the

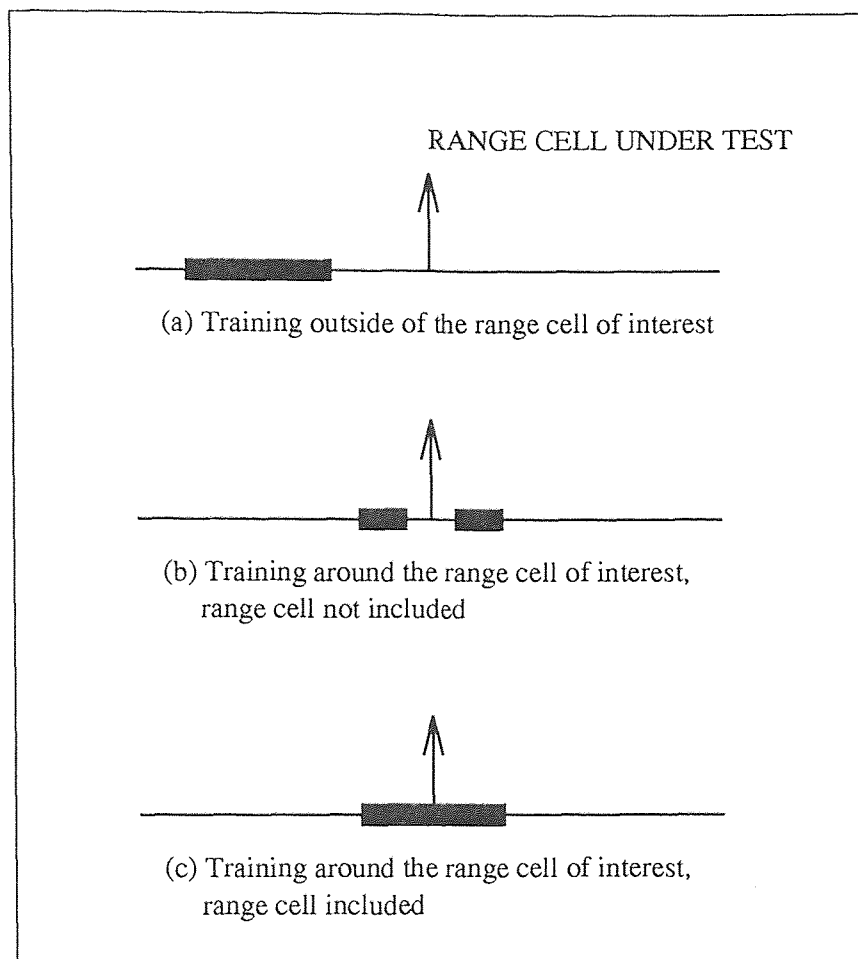


Figure 3.1 Training Regions of the Correlation Matrix

correlation matrix can be expressed in terms of the eigen-decomposition,

$$\widehat{\mathbf{R}}_x^{-1} = \sum_{l=1}^L \lambda_l^{-1} \mathbf{q}_l \mathbf{q}_l^H. \quad (3.3)$$

The eigenvectors are orthonormal,

$$\mathbf{q}_l^H \mathbf{q}_n = \begin{cases} 1 & l = n \\ 0 & l \neq n, \end{cases} \quad (3.4)$$

and form a complete set that spans an L -dimensional space:

$$\sum_{l=1}^L \mathbf{q}_l \mathbf{q}_l^H = \mathbf{I}. \quad (3.5)$$

The signal free covariance matrix is comprised of the interference and the noise contributions. If the covariance matrix is characterized by $r < L$ large eigenvalues then the r associated eigenvectors span the interference subspace. The matrix representation of the interference subspace is obtained by using the first r eigenvectors corresponding to the largest eigenvalues. The matrix representation of the noise subspace is formed using the remaining $L - r$ eigenvectors. The two matrices are formed as follows:

$$\mathbf{Q}_i = \begin{bmatrix} \mathbf{q}_1 & \mathbf{q}_2 & \cdots & \mathbf{q}_r \end{bmatrix}, \quad \text{and} \quad \mathbf{Q}_n = \begin{bmatrix} \mathbf{q}_{r+1} & \mathbf{q}_{r+2} & \cdots & \mathbf{q}_L \end{bmatrix}. \quad (3.6)$$

The interference eigenvalues are used to form an $r \times r$ matrix, $\mathbf{\Lambda}_i$, and the noise eigenvalues are used to form an $(L - r) \times (L - r)$ matrix, $\mathbf{\Lambda}_n$, as follows:

$$\mathbf{\Lambda}_i = \begin{bmatrix} \lambda_1 & 0 & \cdots & 0 \\ 0 & \lambda_2 & \cdots & 0 \\ \vdots & \vdots & \ddots & \vdots \\ 0 & 0 & \cdots & \lambda_r \end{bmatrix} \quad \text{and} \quad \mathbf{\Lambda}_n = \begin{bmatrix} \lambda_{r+1} & 0 & \cdots & 0 \\ 0 & \lambda_{r+2} & \cdots & 0 \\ \vdots & \vdots & \ddots & \vdots \\ 0 & 0 & \cdots & \lambda_L \end{bmatrix}. \quad (3.7)$$

Using \mathbf{Q}_i , \mathbf{Q}_n , $\mathbf{\Lambda}_i$ and $\mathbf{\Lambda}_n$, desired signal free $\widehat{\mathbf{R}}_x$ can be expressed as

$$\widehat{\mathbf{R}}_x = \mathbf{Q}_i \mathbf{\Lambda}_i \mathbf{Q}_i^H + \mathbf{Q}_n \mathbf{\Lambda}_n \mathbf{Q}_n^H. \quad (3.8)$$

3.2 Non Adaptive Beamformer

The non-adaptive beamformer uses the weight vector

$$\mathbf{w}_{non} = \mathbf{s}_m, \quad (3.9)$$

where \mathbf{s}_m is the presumed steering vector for the target. For a given angle, velocity, and type of processor, \mathbf{s}_m has the form of equation (1.9) or equation (1.10). Windowing functions (amplitude taper) maybe used on the steering vector to lower the sidelobes at the cost of increasing the width of the mainlobe. The non-adaptive beamformer maximizes the beamformer's output signal-to-noise ratio in the absence of the interferences.

3.3 Sample Matrix Inversion

Sample matrix inversion (SMI) uses the weight vector

$$\mathbf{w}_{smi} = k \widehat{\mathbf{R}}_x^{-1} \mathbf{s}_m, \quad (3.10)$$

where $\widehat{\mathbf{R}}_x$ is the estimated correlation matrix of the interference and k is a gain constant. The theory of SMI was established in a series of publications by Brennan, Mallett, and Reed [15][16]. \mathbf{w}_{smi} has the same form as \mathbf{w}_o in equation (1.23) except the estimated correlation matrix is used. It was shown that \mathbf{w}_o is the optimal solution for the likelihood ratio detector if components of the array vectors are distributed jointly Gaussian and the interference is a stationary process. Under these assumptions \mathbf{w}_o can be viewed as the classical Wiener filter, which is a whitening filter for the interference cascaded with a match filter for the modified desired signal. However, SMI uses the correlation matrix estimated using a finite window of secondary data resulting in a non-optimal solution. If the data is heterogeneous with non-stationary statistics, training on a secondary data set results in a large estimation error. It has been shown that a data length of at least $2L$, where L is the

length of the data vectors [31], is needed for the SMI to converge. This convergence rate is very slow and it might get even larger if the data is not homogeneous.

3.4 Eigencanceler

The eigencanceler uses the weight vector

$$\mathbf{w}_{\text{eig}} = k\mathbf{Q}_n\mathbf{Q}_n^H\mathbf{s}_m = k(\mathbf{I} - \mathbf{Q}_i\mathbf{Q}_i^H)\mathbf{s}_m, \quad (3.11)$$

where k is a gain constant, \mathbf{s}_m is the presumed steering vector, and \mathbf{Q}_n is the noise subspace. The eigencanceler is a suboptimal beamformer that focuses on the noise subspace. Unlike the optimal solution that equalizes the subspaces with the inverse of the eigenvalues, the eigencanceler nulls out the interference subspace and works on the noise subspace only. This results in superior cancellation and a fast convergence rate.

3.5 Array Improvement Factor Calculations

In this section the effects of calibration errors in terms of the AIF dependency on the desired signal component of the correlation matrix are studied. For analytical tractability, the special case of a single interference and the spatial processor is considered. The results are provided in terms of the SNR, INR, and the projections between the desired, presumed and interference steering vectors.

Consider the estimated correlation matrix given by

$$\widehat{\mathbf{R}}_x = \sigma_d^2\mathbf{s}_d\mathbf{s}_d^H + \sigma_i^2\mathbf{s}_i\mathbf{s}_i^H + (\sigma_n^2/L)\mathbf{I}, \quad (3.12)$$

where σ_d^2 , σ_i^2 , σ_n^2 are desired signal, interference and noise power, and \mathbf{s}_d and \mathbf{s}_i are desired signal and interference vectors, respectively. For the spatial processor the

presumed steering vector has the form of equation (1.9),

$$\mathbf{s}_m = \sqrt{1/L} \begin{bmatrix} 1 \\ e^{j2\pi\psi_m} \\ \vdots \\ e^{j2\pi(L-1)\psi_m} \end{bmatrix}, \quad (3.13)$$

where L is the number of antenna elements. ψ_m is the normalized spatial frequency of the presumed look direction, and it is related to the presumed target angle, θ_m , by equation (1.6). The desired signal vector has the form

$$\mathbf{s}_d = \frac{1}{|c|} \begin{bmatrix} c_0 \\ c_1 e^{j2\pi\psi_d} \\ \vdots \\ c_{L-1} e^{j2\pi(L-1)\psi_d} \end{bmatrix} \quad \text{and} \quad \mathbf{c} = \begin{bmatrix} c_0 \\ c_1 \\ \vdots \\ c_{L-1} \end{bmatrix}, \quad (3.14)$$

where c is a complex random variable with Gaussian-distributed magnitude and phase. The vector \mathbf{c} is used to model the amplitude and phase errors. Assuming good calibration, both the magnitude and the phase of c_l have small variance. The mean of the magnitude is $\sqrt{1/L}$ and the mean of the phase error is zero. In case of the ideal calibration, $c_l = \sqrt{1/L}$. The difference between the true target angle and presumed target angle, $\theta_m - \theta_d$, is the pointing error. Under ideal conditions (no errors), the desired signal vector equals the presumed steering vector. Since the interference signal goes through the same channels as the desired signal, the interference steering vector has the form

$$\mathbf{s}_i = \frac{1}{|c|} \begin{bmatrix} c_0 \\ c_1 e^{j2\pi\psi_i} \\ \vdots \\ c_{L-1} e^{j2\pi(L-1)\psi_i} \end{bmatrix}, \quad (3.15)$$

where ψ_i is the normalized spatial frequency of the interference. The projections between the steering vectors are defined as

$$\rho_{md} = \mathbf{s}_m^H \mathbf{s}_d, \quad \rho_{mi} = \mathbf{s}_m^H \mathbf{s}_i \quad \text{and} \quad \rho_{id} = \mathbf{s}_i^H \mathbf{s}_d. \quad (3.16)$$

Without loss of generality, assume $\sigma_n^2 = L$. Then, $\widehat{\mathbf{R}}_x$ can be written as

$$\widehat{\mathbf{R}}_x = \sigma_d^2 \mathbf{s}_d \mathbf{s}_d^H + \sigma_i^2 \mathbf{s}_i \mathbf{s}_i^H + \mathbf{I} \quad (3.17)$$

In terms of its eigenvectors, $\widehat{\mathbf{R}}_x$ is given by

$$\widehat{\mathbf{R}}_x = (\lambda_1 - 1)\mathbf{q}_1\mathbf{q}_1^H + (\lambda_2 - 1)\mathbf{q}_2\mathbf{q}_2^H + \mathbf{I}, \quad (3.18)$$

where \mathbf{q}_l is the l^{th} eigenvector and λ_l is the l^{th} eigenvalue for $l \in [1, 2]$. For $l \in [3, L]$, the eigenvalues are equal to 1. The signal-plus-interference subspace is 2-dimensional and the noise subspace is $(L - 2)$ -dimensional. Using σ_i^2 , σ_d^2 , and ρ_{id} (see Appendix A), first two eigenvalues of $\widehat{\mathbf{R}}_x$ are given by

$$\lambda_{1,2} = \frac{\sigma_i^2 + \sigma_d^2}{2} \left(1 \pm \sqrt{1 - \frac{4\sigma_i^2\sigma_d^2(1 - |\rho_{id}|^2)}{(\sigma_i^2 + \sigma_d^2)^2}} \right) + 1. \quad (3.19)$$

The eigenvectors corresponding to these eigenvalues are given by

$$\mathbf{q}_{1,2} = \frac{\mathbf{s}_d + \alpha_{1,2}\mathbf{s}_i}{\sqrt{1 + |\alpha_{1,2}|^2 + 2\text{Re}(\alpha_{1,2}\rho_{id}^*)}}, \quad (3.20)$$

where α is

$$\alpha_{1,2} = \frac{\lambda_{1,2} - \sigma_d^2}{\sigma_d^2\rho_{id}^*} = \frac{\sigma_i^2\rho_{id}}{\lambda_{1,2} - \sigma_i^2}. \quad (3.21)$$

The inverse of the estimated correlation matrix is given by

$$\widehat{\mathbf{R}}_x^{-1} = \mathbf{I} - \beta_1\mathbf{q}_1\mathbf{q}_1^H - \beta_2\mathbf{q}_2\mathbf{q}_2^H, \quad (3.22)$$

where

$$\beta_{1,2} = \frac{\lambda_{1,2} - 1}{\lambda_{1,2}}. \quad (3.23)$$

The AIF for SMI is calculated using equations (1.21) and (3.10) as follows:

$$G_{smi} = \frac{|\mathbf{s}_m^H \widehat{\mathbf{R}}_x^{-1} \mathbf{s}_d|^2}{\mathbf{s}_m^H \widehat{\mathbf{R}}_x^{-1} \mathbf{R}_{i+n} \widehat{\mathbf{R}}_x^{-1} \mathbf{s}_m}, \quad (3.24)$$

where

$$\mathbf{R}_{i+n} = \sigma_i^2 \mathbf{s}_i \mathbf{s}_i^H + \mathbf{I}. \quad (3.25)$$

The numerator of G_{smi} is given by

$$\left| \mathbf{s}_m^H \widehat{\mathbf{R}}_x^{-1} \mathbf{s}_d \right|^2 = \left| \rho_{md} - \beta_1 \mathbf{s}_m^H \mathbf{q}_1 \mathbf{q}_1^H \mathbf{s}_d - \beta_2 \mathbf{s}_m^H \mathbf{q}_2 \mathbf{q}_2^H \mathbf{s}_d \right|^2, \quad (3.26)$$

and the denominator is given by

$$\begin{aligned}
\mathbf{s}_m^H \widehat{\mathbf{R}}_x^{-1} \mathbf{R}_{i+n} \widehat{\mathbf{R}}_x^{-1} \mathbf{s}_m = & 1 + \sigma_i^2 |\rho_{mi}|^2 \\
& + (\beta_1^2 - 2\beta_1 + \beta_1^2 \sigma_i^2 |\mathbf{q}_1^H \mathbf{s}_i|^2) \mathbf{s}_m^H \mathbf{q}_1 \mathbf{q}_1^H \mathbf{s}_m \\
& + (\beta_2^2 - 2\beta_2 + \beta_2^2 \sigma_i^2 |\mathbf{q}_2^H \mathbf{s}_i|^2) \mathbf{s}_m^H \mathbf{q}_2 \mathbf{q}_2^H \mathbf{s}_m \\
& + 2\beta_1 \beta_2 \sigma_i^2 \text{Re}(\mathbf{s}_m^H \mathbf{q}_1 \mathbf{q}_1^H \mathbf{s}_s \mathbf{s}_s^H \mathbf{q}_2 \mathbf{q}_2^H \mathbf{s}_m) \\
& - 2\sigma_i^2 \beta_1 \text{Re}(\mathbf{s}_s^H \mathbf{q}_1 \mathbf{q}_1^H \mathbf{s}_m \rho_{mi}) \\
& - 2\sigma_i^2 \beta_2 \text{Re}(\mathbf{s}_s^H \mathbf{q}_2 \mathbf{q}_2^H \mathbf{s}_m \rho_{mi}).
\end{aligned} \tag{3.27}$$

In the same manner, the array gain for the eigencanceler is calculated using equations (1.21), (3.11) and (3.6), with $r = 1$ (single interference), as follows:

$$G_{eig} = \frac{|\mathbf{s}_m^H (\mathbf{I} - \mathbf{q}_1 \mathbf{q}_1^H) \mathbf{s}_d|^2}{\mathbf{s}_m^H (\mathbf{I} - \mathbf{q}_1 \mathbf{q}_1^H) \mathbf{R}_{i+n} (\mathbf{I} - \mathbf{q}_1 \mathbf{q}_1^H) \mathbf{s}_m}. \tag{3.28}$$

The numerator of G_{eig} is given by

$$|\mathbf{s}_m^H (\mathbf{I} - \mathbf{q}_1 \mathbf{q}_1^H) \mathbf{s}_d|^2 = |\rho_{md} - \mathbf{s}_m^H \mathbf{q}_1 \mathbf{q}_1^H \mathbf{s}_d|^2, \tag{3.29}$$

and the denominator is given by

$$\mathbf{w}_{eig}^H \mathbf{R}_{i+n} \mathbf{w}_{eig} = 1 + \sigma_i^2 |\rho_{mi}|^2 + (\sigma_i^2 |\mathbf{s}_i^H \mathbf{q}_1|^2 - 1) |\mathbf{s}_m^H \mathbf{q}_1|^2 - 2 \text{Re}(\sigma_i^2 \rho_{mi} \mathbf{s}_i^H \mathbf{q}_1 \mathbf{q}_1^H \mathbf{s}_m). \tag{3.30}$$

To study the effects of the SNR, INR, calibration and pointing errors, the G_{smi} and G_{eig} are plotted. For all of the plots $\sigma_n^2 = L$, where $L = 14$, and the G_{smi} and G_{eig} are normalized by L .

In Figure 3.2, G_{smi} and G_{eig} are plotted as a function of the presumed target angle, θ_d , for the case of ideal phase and gain calibration, $c_i = \sqrt{1/L}$. In Figure 3.2(a), the correlation matrix has no signal component, $\sigma_d^2 = 0$. Under these conditions, SMI is the optimal solution, since $\widehat{\mathbf{R}}_x$ is the true correlation matrix of the interference and Gaussian noise. The G_{smi} and G_{eig} overlap for $\sigma_i^2 = 1400$ ($INR = 20$ dB). In Figure 3.2(b) the desired signal component is present in the correlation matrix, $\sigma_d^2 = 140$ ($SNR = 10$ dB). For this case, SMI works only if $\theta_m = \theta_d$. A slight pointing error causes a large decrease in the AIF. The eigencanceler, however, is much less affected by the increase of the SNR.

In Figure 3.3, effects of the phase errors, and pointing error are studied. There are no amplitude errors, $|c_l| = \sqrt{1/L}$, and the phase errors are modeled as a zero-mean Gaussian random variable. Phase errors are averaged over 50 iterations. As the standard deviation (STD) of the phase errors increases, G_{smi} starts to decrease, due to the mismatch between the desired and presumed steering vectors. The mainlobe is again very narrow due to the presence of the desired signal. The eigencanceler is very robust against the phase errors as seen in Figure 3.3(b), where the mainlobe is hardly changed even for high phase errors.

In Figure 3.4, effects of the amplitude errors and pointing error are investigated. There are no phase errors, $\angle c_l = 0$. The STD of the amplitude errors are normalized by the mean of the amplitude, which is $1/\sqrt{L}$. Again the SMI method performs if there are no pointing errors and the STD of the amplitude errors are very small. Performance is degraded, however, if the STD of amplitude errors are increased or a small pointing error is introduced. The eigencanceler is again robust with respect to amplitude errors and maintains the ideal shape for the mainlobe shape even with amplitude errors of 10% STD from the mean. To generate these plots, 50 iterations are used for every point.

In Figure 3.5, effects of the desired signal power, σ_d^2 , on the pointing error is studied. There are no phase and amplitude errors, $c_l = \sqrt{1/L}$. When the $\sigma_d^2 = 0$, both G_{smi} and G_{eig} have the same mainlobe as Figure 3.2(a), which is the ideal solution. As the desired signal power is increased, the SMI's mainlobe becomes narrower and the performance is decreased for even a small pointing error. The eigencanceler's performance is acceptable up to a SNR of 10 dB, but G_{eig} goes down rapidly as the SNR gets closer to the INR. This behavior is due to the shift of the first eigenvector, which starts to look like the desired signal as the SNR approaches the INR. When the SNR is equal to the INR, the eigencanceler fails even when there

are no pointing errors, because the first eigenvector has a large projection on the desired signal, which causes desired signal cancellation.

In Figure 3.6, effects of the desired signal angle on the pointing errors is plotted. The desired signal angle does not have a very significant effect on the shape of the mainlobe. As seen in Figure 3.6(b), the mainlobe gets slightly larger as the desired signal angle is increased. This is due to the nonlinear mapping, from the physical to the electrical angle, given by equation (1.6). As θ_d gets larger, the electrical pointing error is smaller for the same physical pointing error. Therefore, the mainlobe related to the electrical pointing errors becomes larger.

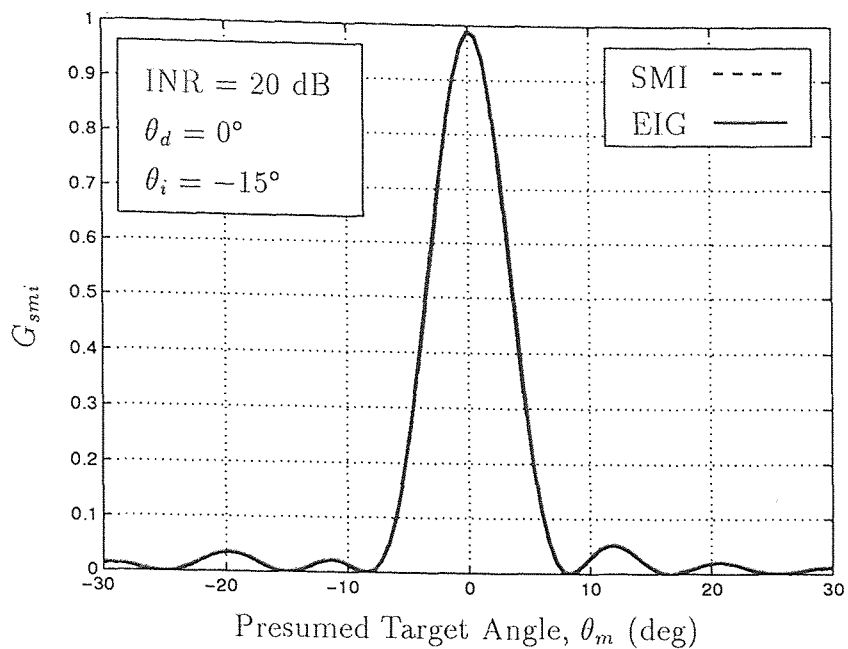
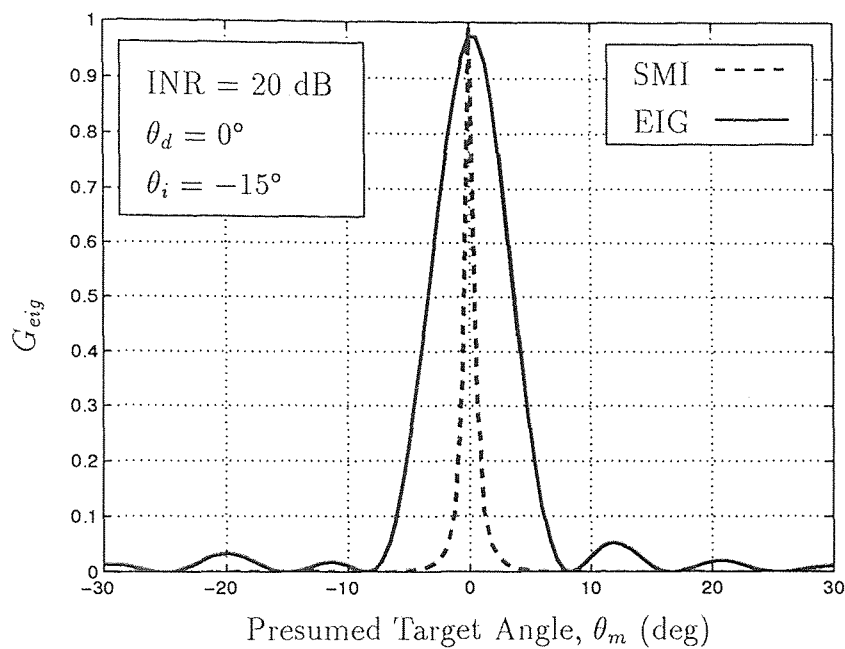
(a) No Desired Signal Component, $\sigma_d^2 = 0$ (b) With Desired Signal Component, $\sigma_d^2 = 10$

Figure 3.2 Effects of Desired Signal Component and Pointing Error on the AIF

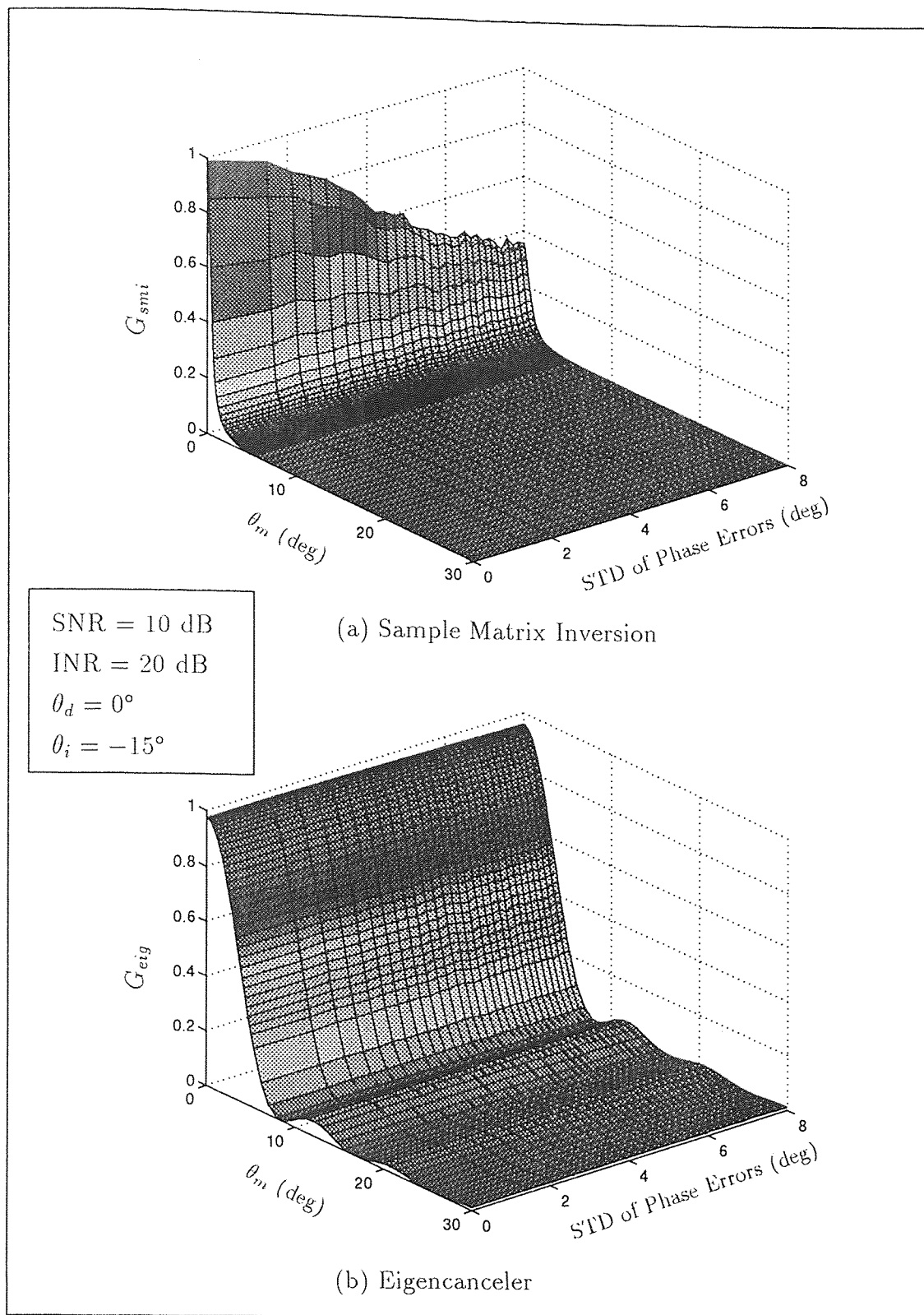


Figure 3.3 Effects of Phase Errors and Pointing Error on the AIF

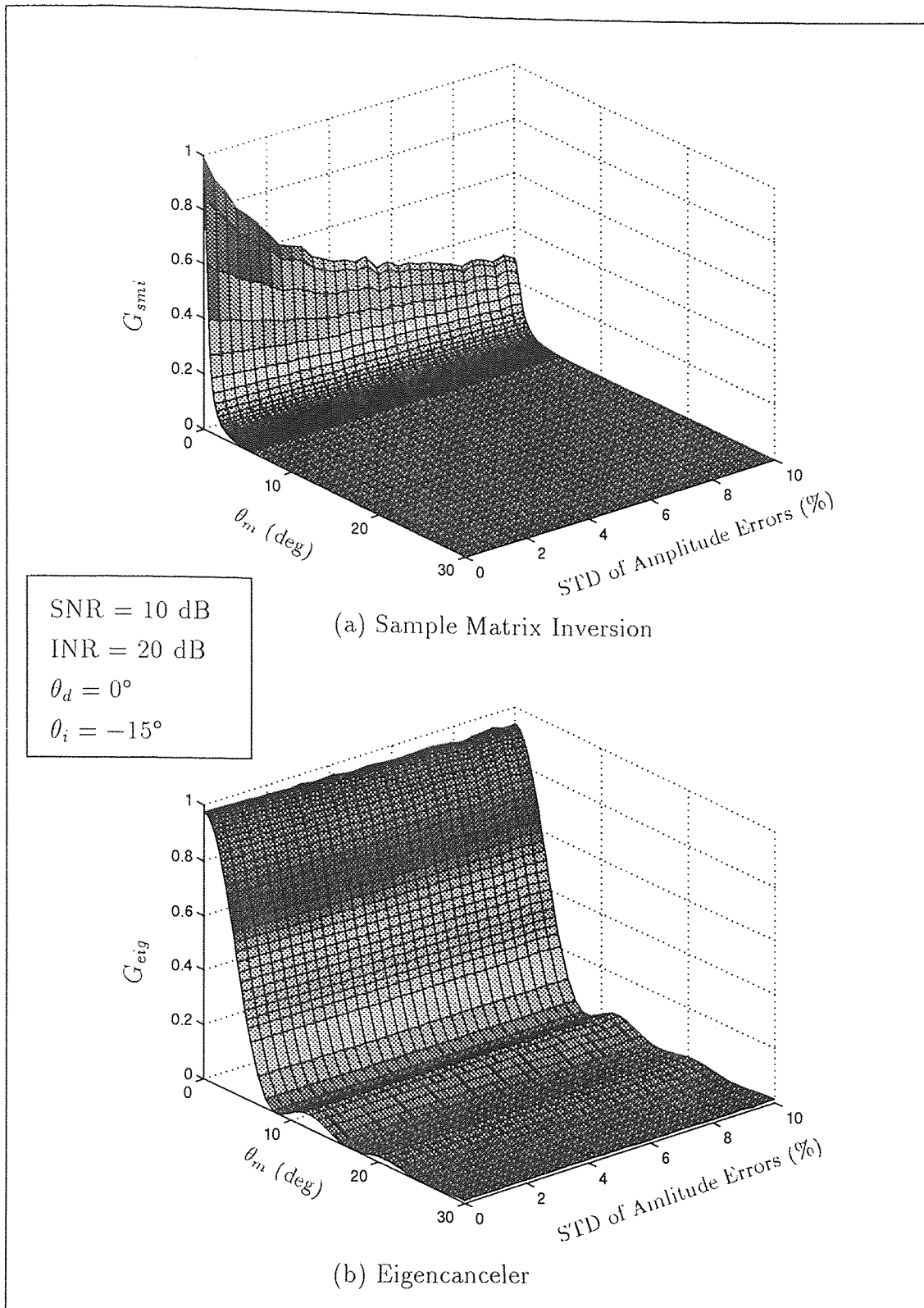


Figure 3.4 Effects of Amplitude Errors and Pointing Error on the AIF

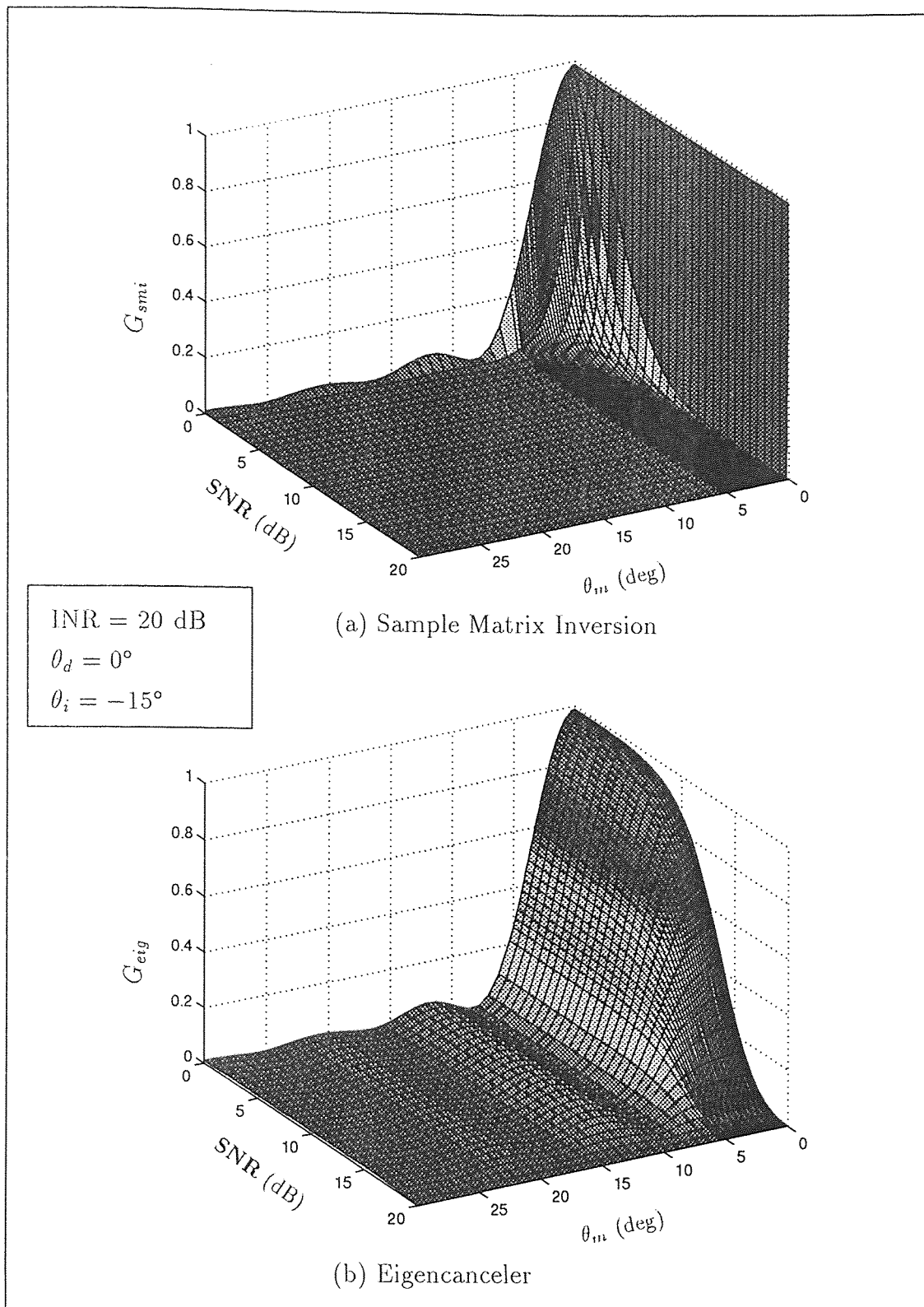


Figure 3.5 Effects of Signal-to-Noise Ratio and Pointing Error on the AIF

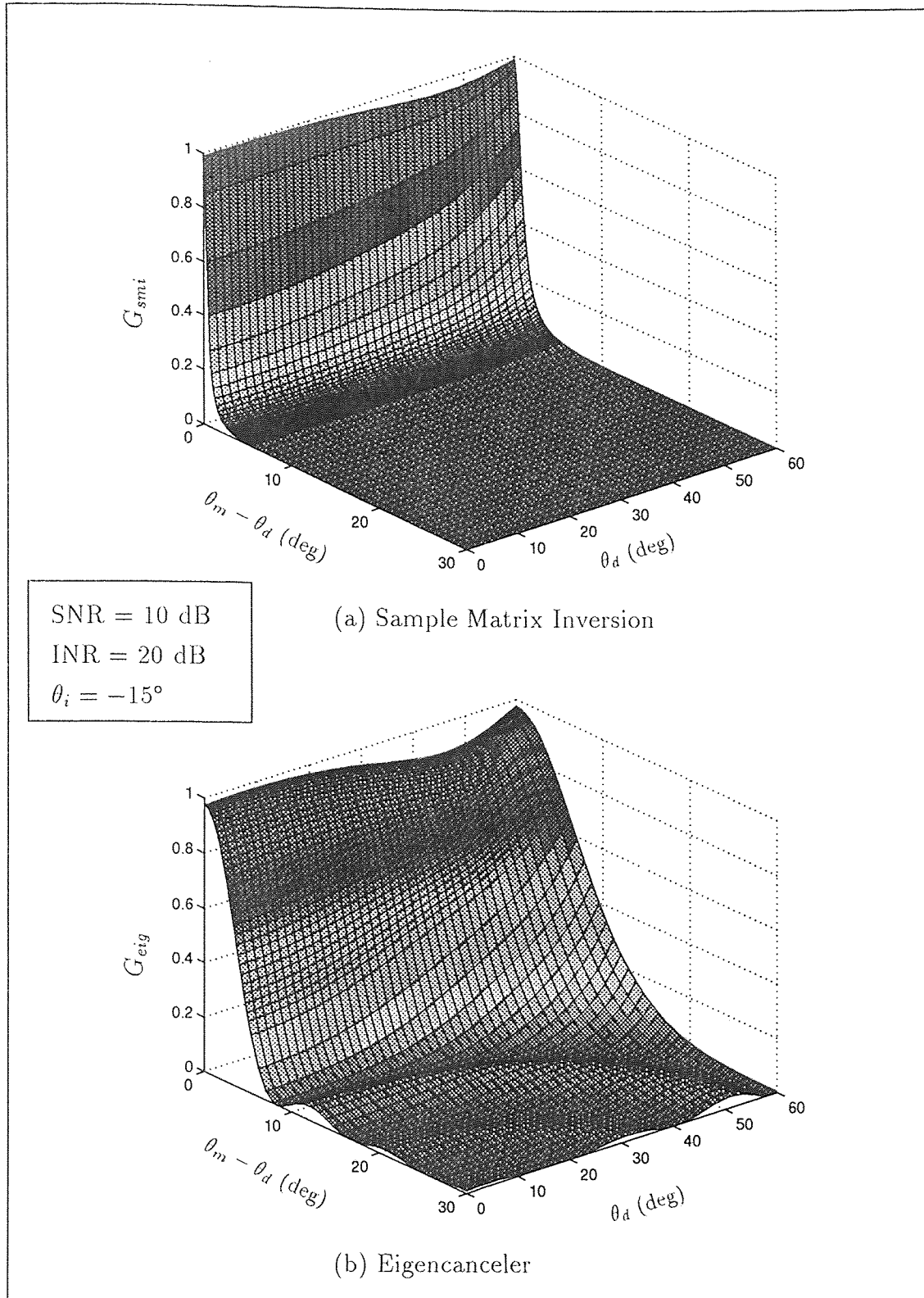


Figure 3.6 Effects of Desired Signal Angle and Pointing Error on the AIF

CHAPTER 4

MOUNTAIN-TOP DATA ANALYSIS

Analytical results presented in the previous chapter show that the eigencanceler is robust with respect to steering vector perturbations. In this chapter, the performance of the eigencanceler and SMI are compared using the Mountaintop dataset. After describing the specific data file used, range detection with corresponding antenna response and angle detection of the target are studied. Training sets of different sizes from different regions are used. The last section considers the signal suppression issue when the cell under test is included in the training.

4.1 Description of the Data Files

Data analysis was done on IDPCA data recorded on Feb 10, 1994 at North Oscura Peak, White Sands Missile Range (WSMR), New Mexico. For this data set, namely t38pre01v1.mat, IDPCA was used to emulate clutter at 245° and 156 Hz in Doppler. The injected target is at 154 km in range, 275° in angle, and 156 Hz in Doppler. The bore side angle is 260° . The transmitted pulse is an LFM signal with 500 KHz of bandwidth, a central frequency of 435 MHz, and a 100 μs duration. Distance between the elements is half the wavelength, $d = \lambda/2$. Recorded data is sampled at the Nyquist rate of 1 MHz. The PRI is 1600 μs , which gives a pulse repetition frequency (PRF) of 625 Hz. Data is recorded from 865 μs to 1298 μs after the pulse is transmitted, corresponding to range cells from 130 km to 195 km with a range resolution of 150 m. Data is recorded into CPI's with 16 PRI's. Using equation (1.7), the normalized Doppler frequency of the target is 0.250. Since 14 antennas are employed, there are 14 samples in space. For each range cell a 16×14 data matrix, as described in equation (1.2), is formed. Using equation (1.6), the normalized spatial frequency of the target is 0.129 and the normalized spatial frequency of the

interference is -0.129 . Notice that both the target and the interference are at the same Doppler frequency, and they are only separated spatially.

Using CPI 6 of the data, the magnitude of the first PRI as a function of range is plotted in Figure 4.1. The returns from the ranges are plotted with respect to the sky noise level. The clutter is located from 140 km to 165 km. In Figure 4.2, the Doppler-azimuth plot of the target range cell at 154 km is plotted. As expected, the energy is concentrated at 156 Hz and 245° due to the interference power. To study the eigenvalue distribution of joint-domain processing, each range matrix is reshaped to a joint-domain data vector of size 224×1 , as described in equation (1.12). To estimate the correlation matrix, 1200 training data vectors from matrix CPI's 6, 7, 8 and 9 were used. The eigenvalues of this correlation matrix are plotted in Figure 4.3(a), where the few interference eigenvalues are well above the sky noise level. For post-Doppler processing, each range data matrix is first processed temporally with the non-adaptive weight vector, which has the form of \mathbf{s}_l in equation (1.9). Then beamforming algorithms are applied to the 14×1 spatial data vectors. The correlation matrix of post-Doppler data is estimated using 300 data points from CPI 6. The eigenvalues are plotted in Figure 4.3(b), where most of the energy is concentrated in the first 4-5 eigenvectors.

4.2 Target Range Detection

In this section, the target angle and Doppler frequency are assumed to be known and the target range is detected. The data is plotted relative to sky noise. Sky noise data, namely `ncal585v1.mat`, is recorded right after the experiment with the transmitter turned off. To calculate the sky noise level at the output of the beamformer, the weights calculated for a specific experiment are applied to the sky noise data. The mean of the sky noise output is taken as the sky noise reference. If the beamformer is adaptive, the weight vector changes with the training region and number of points

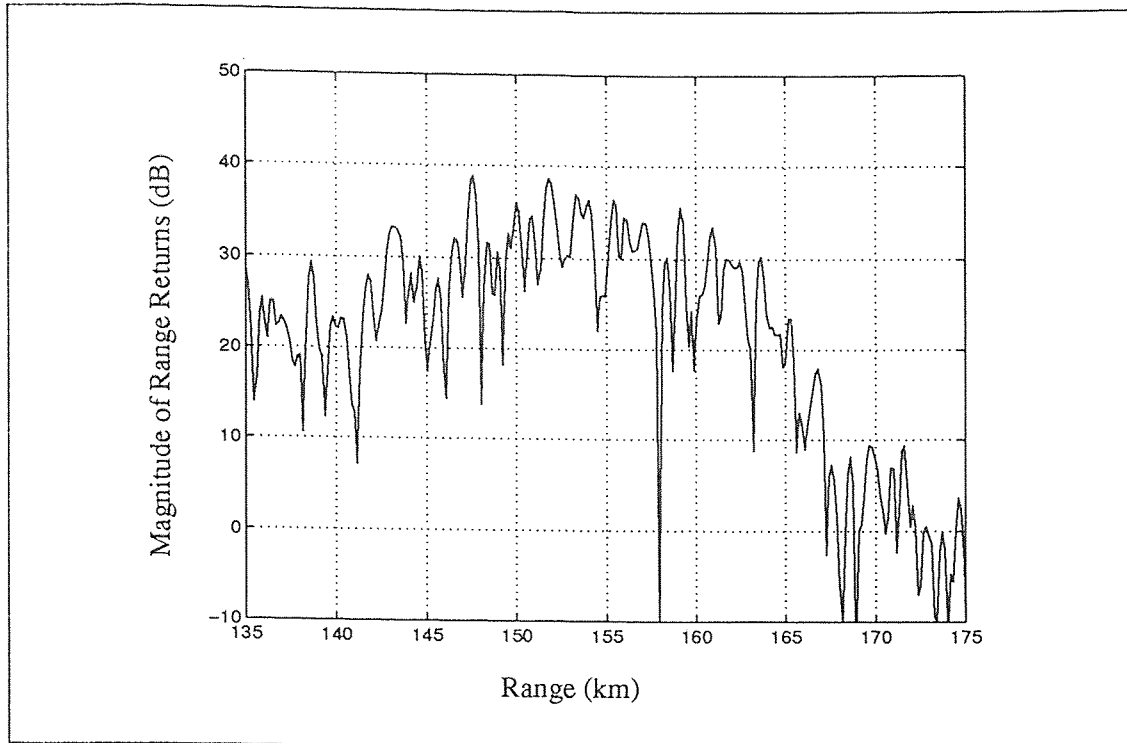


Figure 4.1 Magnitude Plot of Range Returns on IDPCA Data, CPI 6, PRI 1

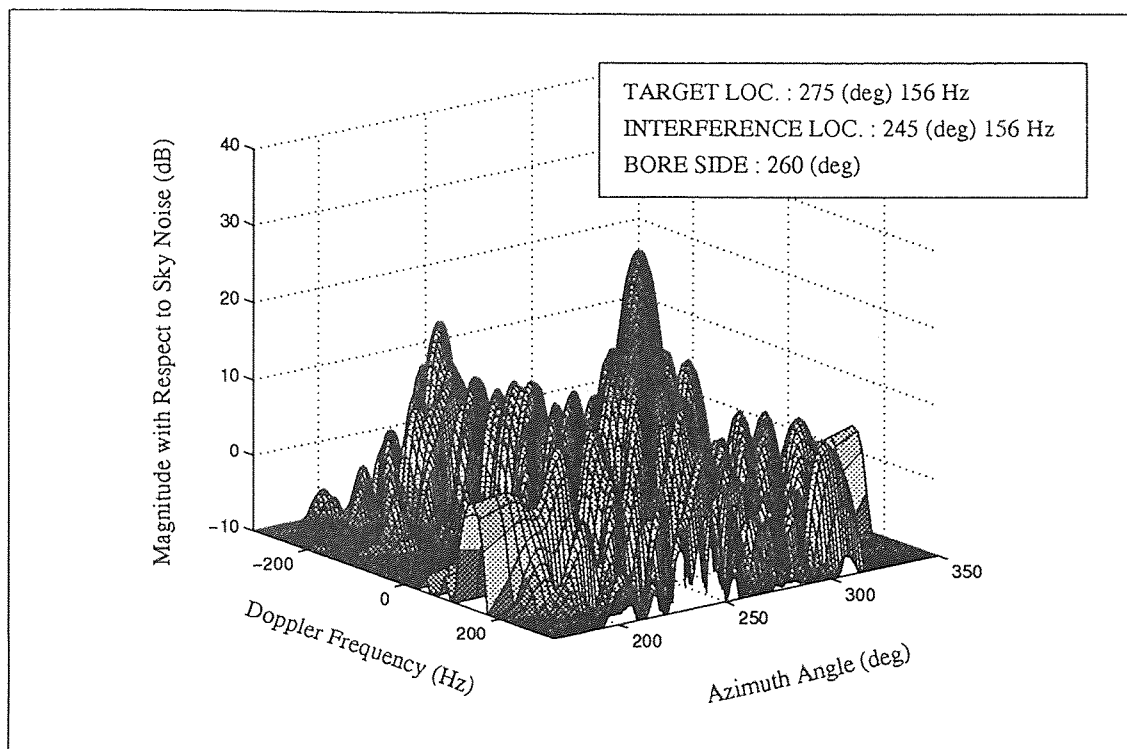


Figure 4.2 Doppler-Azimuth Plot for Target Range Cell

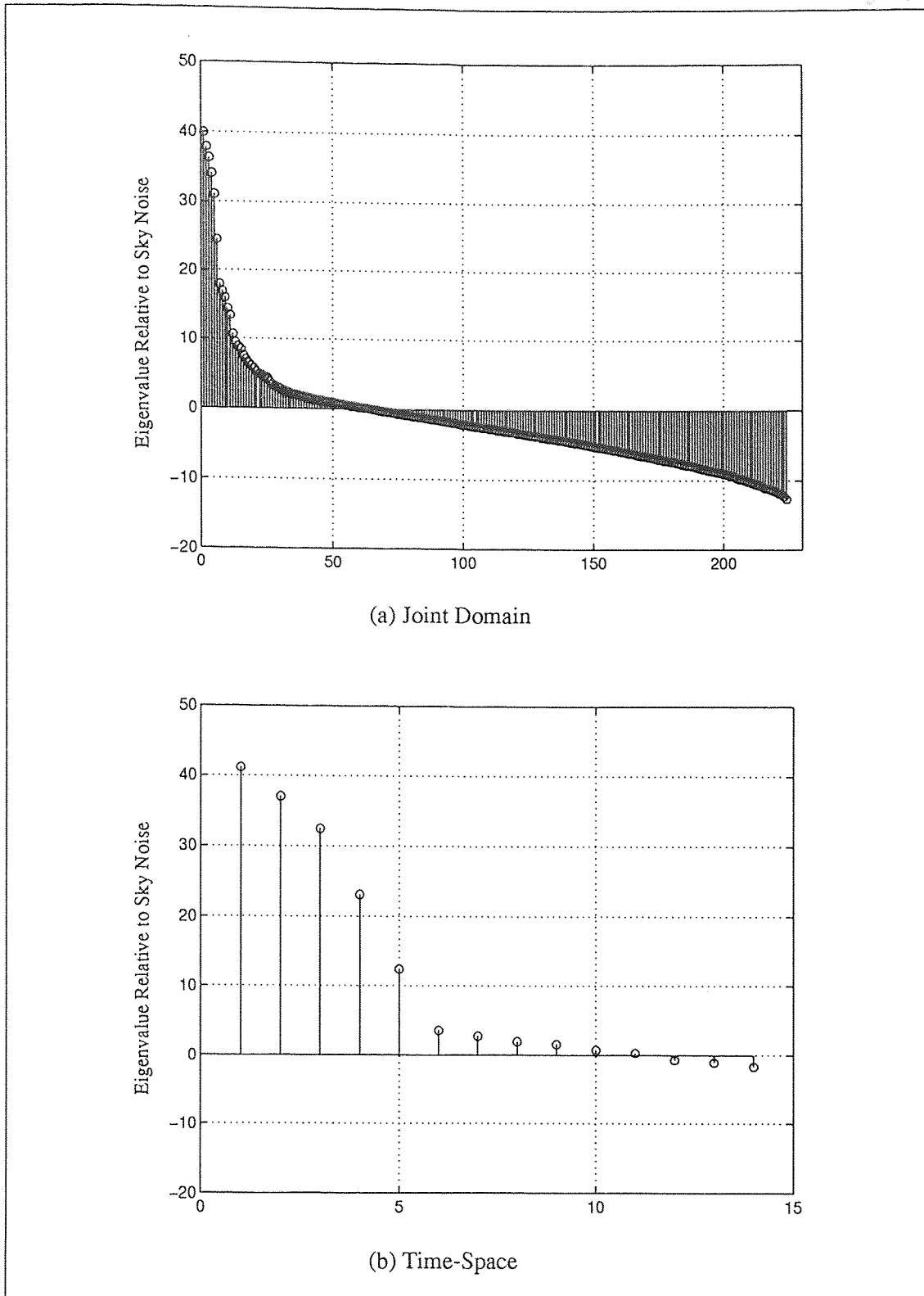


Figure 4.3 Eigenvalues of the Data

used. For every plot, the sky noise level is updated using the corresponding weight vector. For these plots CPI 6 is used, which has 300 data vectors.

First, the joint-domain processor with 14 antenna elements and 4 PRIs is studied. The joint-domain data vector for this case is 56×1 . In Figure 4.4(a), training is done over 300 points from 135 km to 175 km, and the target range cells are excluded from the training set. The target is located at 154 km and the power of the target spills over 5 range cells. Clearly, the non-adaptive beamformer fails due to a large sidelobe. Both SMI and the eigencanceler have the same performance. But this is not a realistic approach since *a-priori* knowledge of the target location was used when estimating the correlation matrix. A more realistic approach is given in Figure 4.4(b), where all the data vectors are used for training, including the target region. Presence of the target region in the training set causes an increase in the desired signal component of the estimated correlation matrix. The SMI method fails to preserve the desired signal, and signal cancellation of 12 dB is observed. Performance of the eigencanceler is not affected by high signal power in the estimate.

Next, the post-Doppler beamformer is studied. After temporal processing, the post-Doppler data vectors are 14×1 . In Figure 4.5(a), training is over 300 data points, and the target region is not included in the estimate. The performance of the post-Doppler processor is better than the joint-domain processor because both the desired signal and the interference have the same Doppler frequency. The joint-domain processor, which is adaptive both in time and space, cancels the interference temporally and spatially. Because the interference and target signal are in the same Doppler bin, some signal power is lost. The post-Doppler processor performs cancellation in the spatial domain, where the target and interference are separated. Therefore, the post-Doppler processor performs better for this specific data set. In Figure 4.5(b), the target region is included in the training. The SMI method is affected by the high desired signal component and the performance is degraded by

7 dB. The eigencanceler, on the other hand, is not affected by the presence of the desired signal, as shown analytically in section 3.5 and plotted in Figure 3.5. In Figure 4.6, training with 50 data points is considered. In part (a), the training is done from 145 km to 152 km, which is outside the target region. Both adaptive methods cancel most of the clutter. The non-adaptive beamformer output does not change due to the fixed weights, and it is plotted again as the clutter reference. An important observation is that the SMI method performs more cancellation around the training region. This is due to the limited number of training samples, which causes a correlation matrix to be a good estimate of the training region, but very bad estimate globally. In parts (b) and (c), the training is done around the target region from 150 km to 158 km. As before, when the target is omitted from the training set, a very good performance is observed. Again the training region is nulled by the SMI method, where the eigencanceler lowers the output but does not null out. In part (c), where the target is included in the training set, the SMI method fails by treating the desired signal as interference. Unlike the SMI, the eigencanceler does not null out the desired signal, but the interference cancellation of the eigencanceler is degraded. Presence of the desired signal shifts the largest eigenvectors towards the desired signal, causing a corrupt estimation of the interference subspace. In Figure 4.7, training with 28 points-double the vector size-is considered. This is the lower limit for SMI to work. In part (a), a deeper null is placed by the SMI method in the training region. The performance of the eigencanceler is better than SMI, which shows that the eigencanceler has a faster convergence rate. In part (c), both methods fail. The signal cancellation problem of the SMI is magnified. The eigencanceler still manages to save some of the signal power, but fails to cancel the interference. In fact, interference cancellation is worse than with the non-adaptive method from 140 km to 150 km.

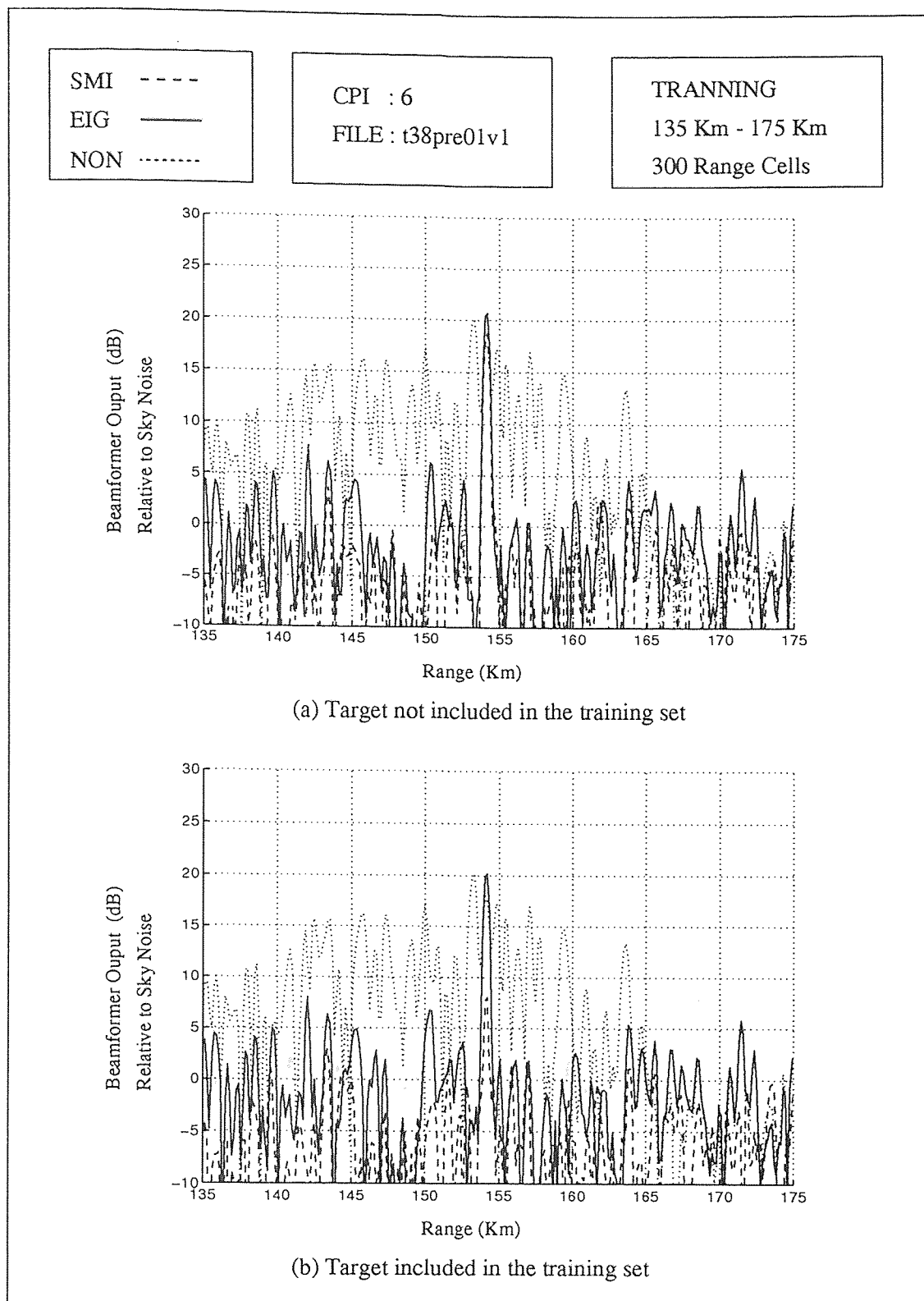


Figure 4.4 Joint-Domain Range Plots Using 300 Training Points

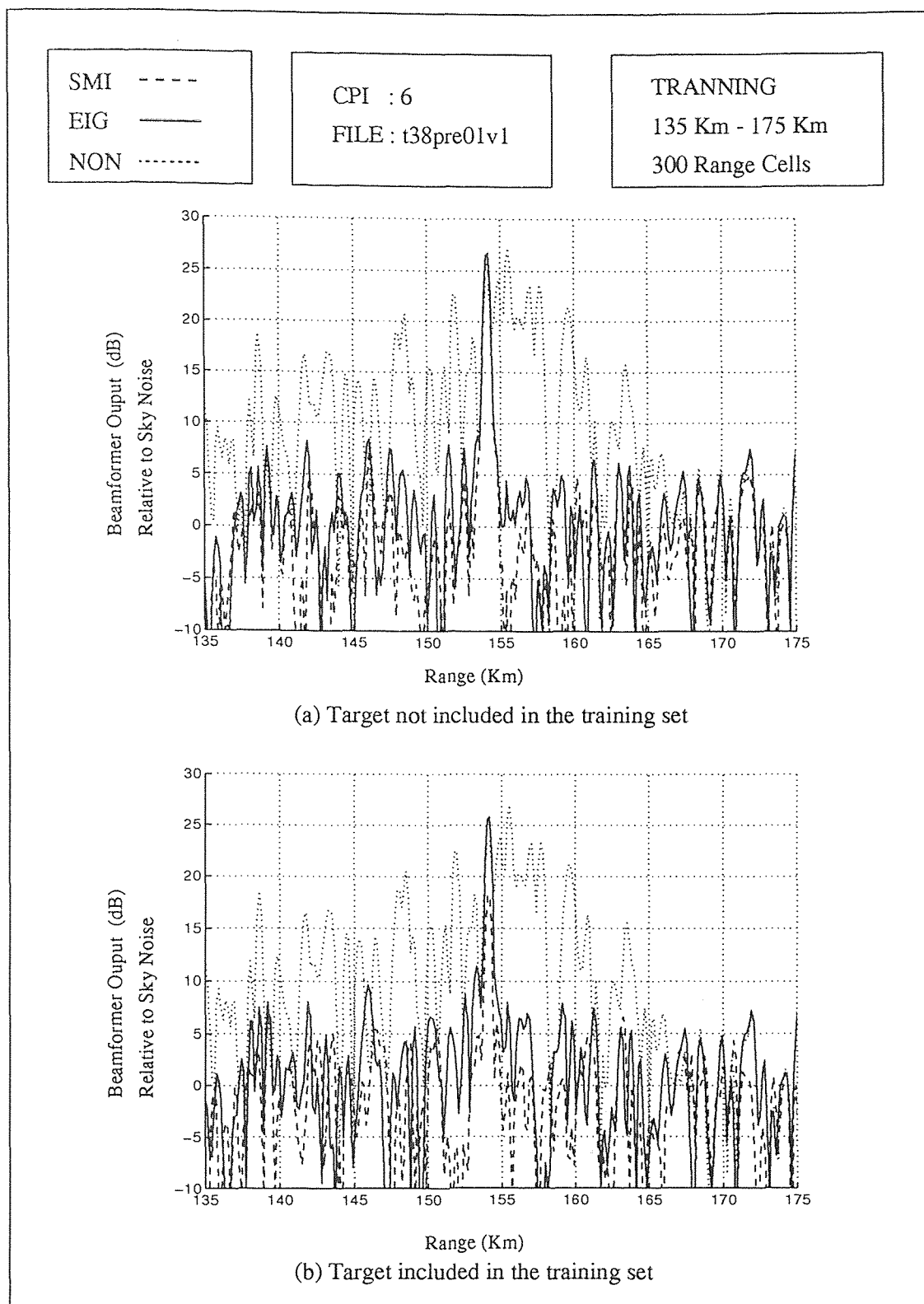


Figure 4.5 Post-Doppler Range Plots Using 300 Training Points

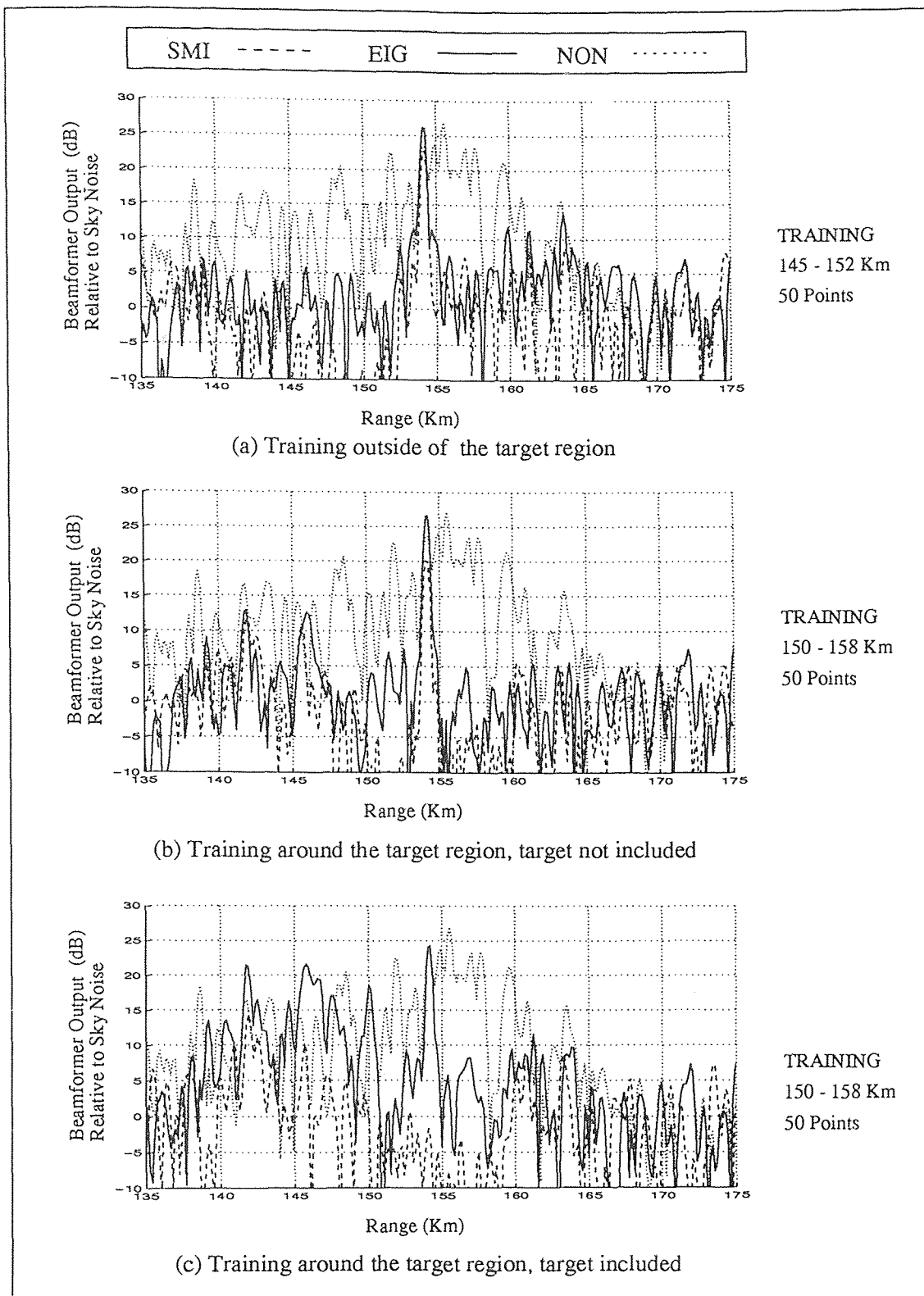


Figure 4.6 Post-Doppler Range Plots Using 50 Training Points

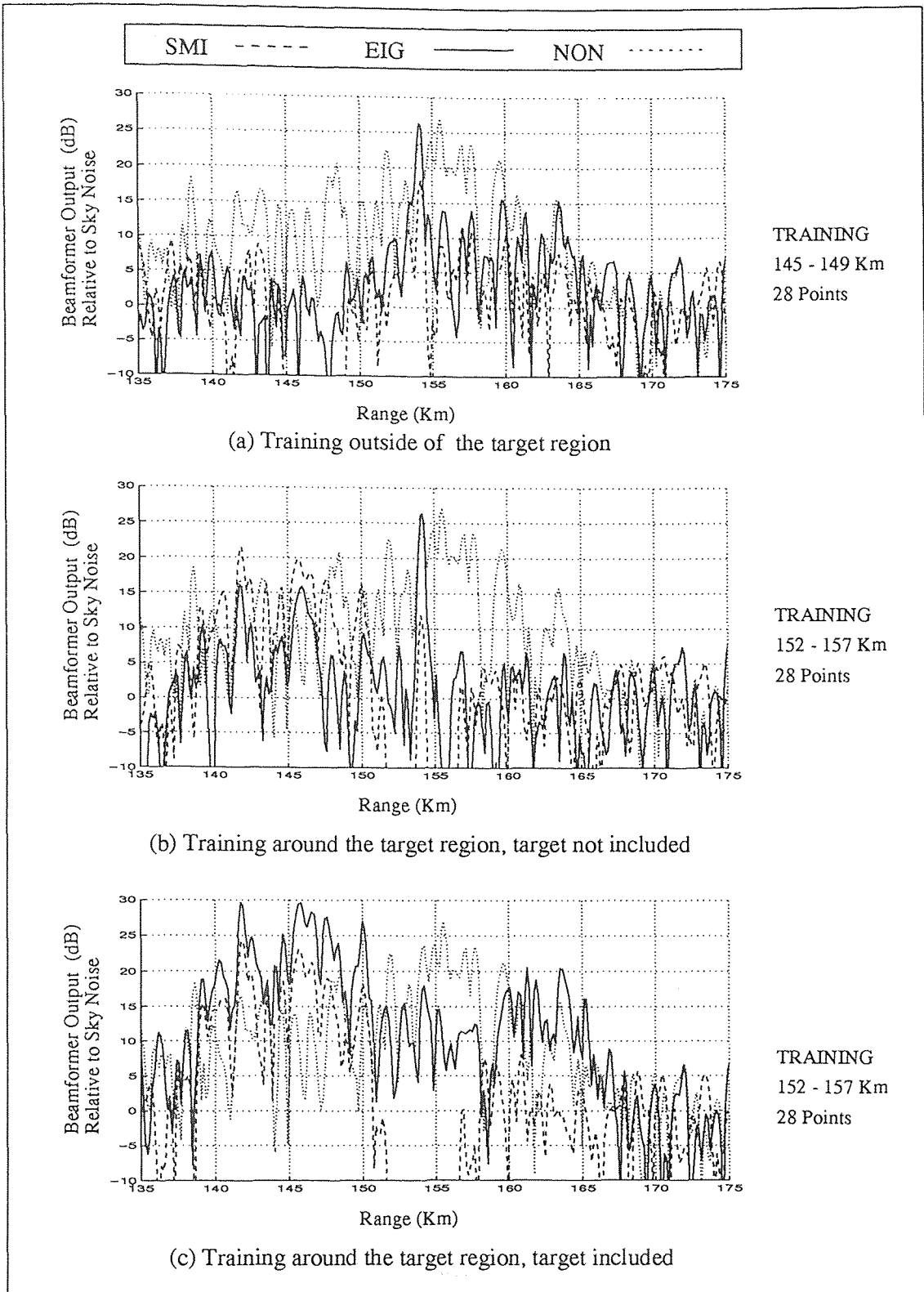


Figure 4.7 Post-Doppler Range Plots Using 28 Training Points

4.3 Antenna Pattern

In this section, the spatial response of the weights calculated for the post-Doppler range plots of the previous section is studied. Assuming an ideal desired signal, the spatial data vector will have the form of \mathbf{s}_s in equation (1.9). The normalized spatial frequency, ψ_s , is related to the physical angle by equation (1.6). The antenna patterns are generated by applying a given weight vector to steering vectors for different angles. A desirable weight vector has a main lobe in the direction of the target and a null in the direction of the interference. In this data set the target angle is 275° and the interference angle is 245° .

In Figure 4.8, the response of the weight vectors calculated with 300 training points are plotted. The non-adaptive weight vector, plotted for reference, is the presumed steering vector for the desired signal. Around the interference angle, both adaptive beamformers have a lower sidelobe than the non-adaptive beamformer. In part (b), the target region included in the estimate, the SMI method puts a small notch on the main lobe causing the performance degradation observed in the range plots of the previous section. The eigencanceler's sidelobes resemble the non-adaptive weight vector, except in the interference region. Comparing both parts, the eigencanceler is not affected by the presence of the desired signal in the estimate.

In Figure 4.9, the response of the weight vector calculated with 50 training points is plotted. In part (a), a decrease in the training set number has affected the SMI method with increased sidelobes, but the eigencanceler manages to keep the same shape. Even though interference cancellation of the eigencanceler is degraded, we also observe from range plot for the same training that the main lobe is still in the right direction and the sidelobes are relatively low, keeping the shape of the steering vector. Compared to part (b) of the previous figure, the small notch introduced by SMI on the desired signal in part (c) is even deeper.

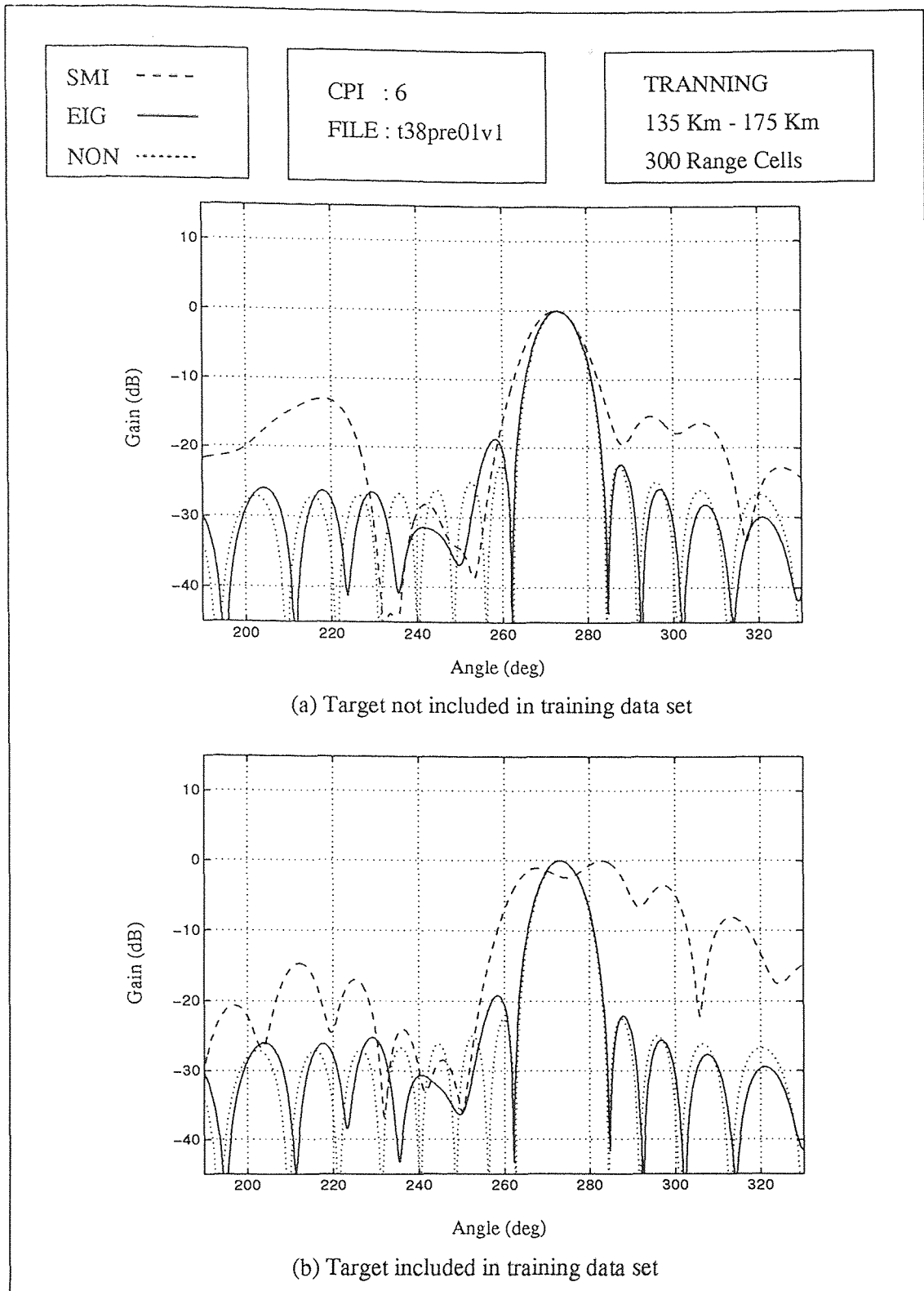


Figure 4.8 Post-Doppler Antenna Pattern Plots Using 300 Training Points

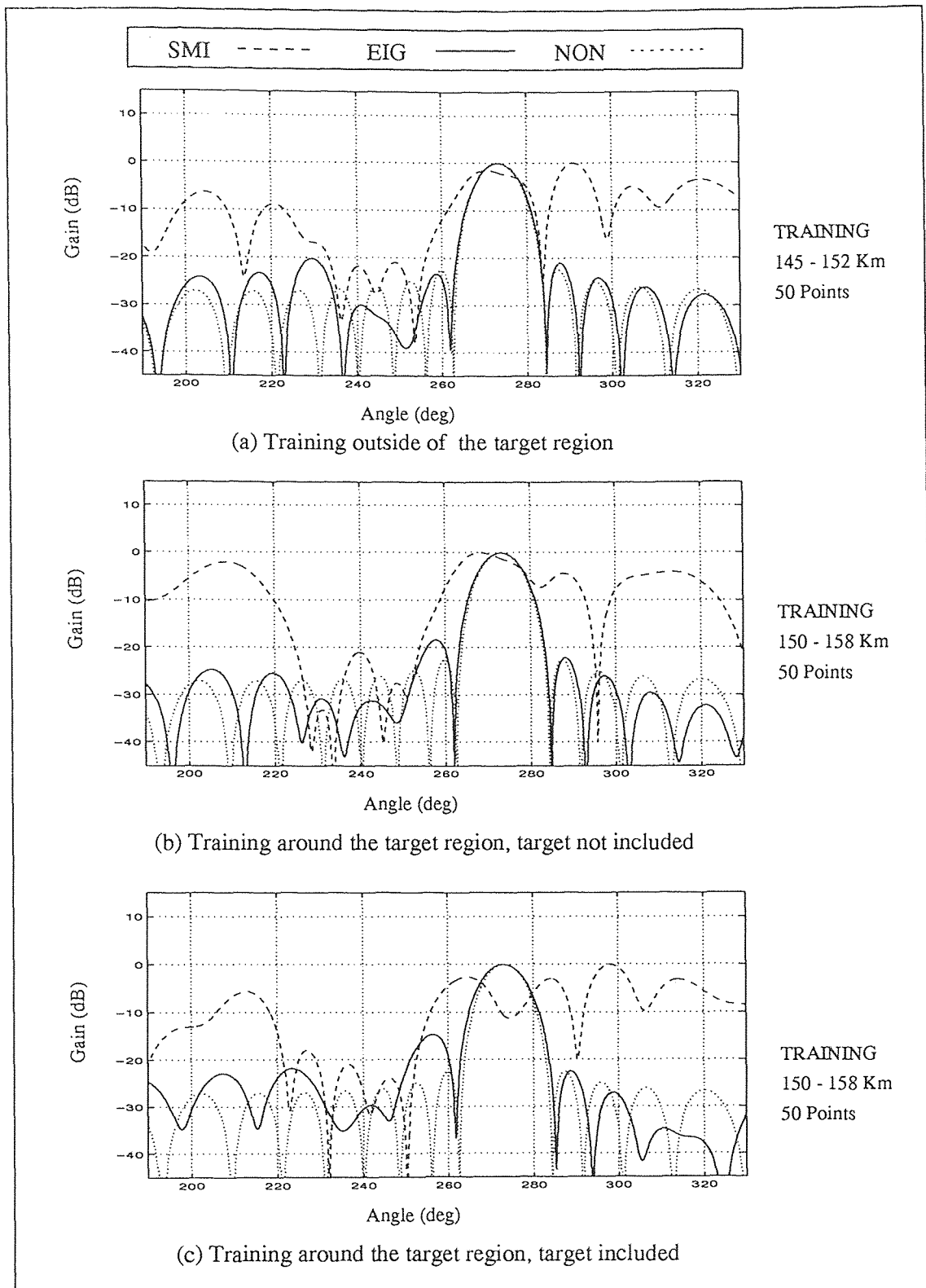


Figure 4.9 Post-Doppler Antenna Pattern Plots Using 50 Training Points

When the training set is lowered to 28 range cells, see Figure 4.10, the SMI method does not give a desirable antenna pattern even for the case of training outside of the target region. The eigencanceler's performance is still preserved in part (a). In addition, as mentioned before for the range plots with the target included in training in part (c), both adaptive methods fail and performance is worse than the non-adaptive beamformer.

4.4 Target Angle Detection

In this section, the target range and the Doppler frequency are assumed to be known, and the target angle is detected. The post-Doppler data vector for the target range cell at 154 km is used to detect the target angle. First the correlation matrix is estimated for a given training region, and then the weight vectors are calculated using different presumed desired signal angles. For this data set, the target is at 245° . In Figure 4.11, the training is done using all 300 range cells. The non-adaptive beamformer fails, due to a large sidelobe, and points in the direction of the interference. Both SMI and the eigencanceler detect the right angle for the target. When the training is lowered to 50 cells, see Figure 4.12, the sidelobes of the SMI are increased. The performance of the eigencanceler is almost unchanged. In Figure 4.13, the training support is lowered to 28 cells. The performance of SMI is degraded considerably and the eigencanceler's performance is superior. Even with the target included in the training set, the eigencanceler manages to detect the target, even though it is only a few dB above the interference. The sidelobes of the eigencanceler are much lower than the sidelobes of the SMI.

4.5 Signal Cancellation

In this section, signal cancellation due to the high desired signal component of the estimated correlation matrix is studied. In Figure 4.14(a), the target range cell

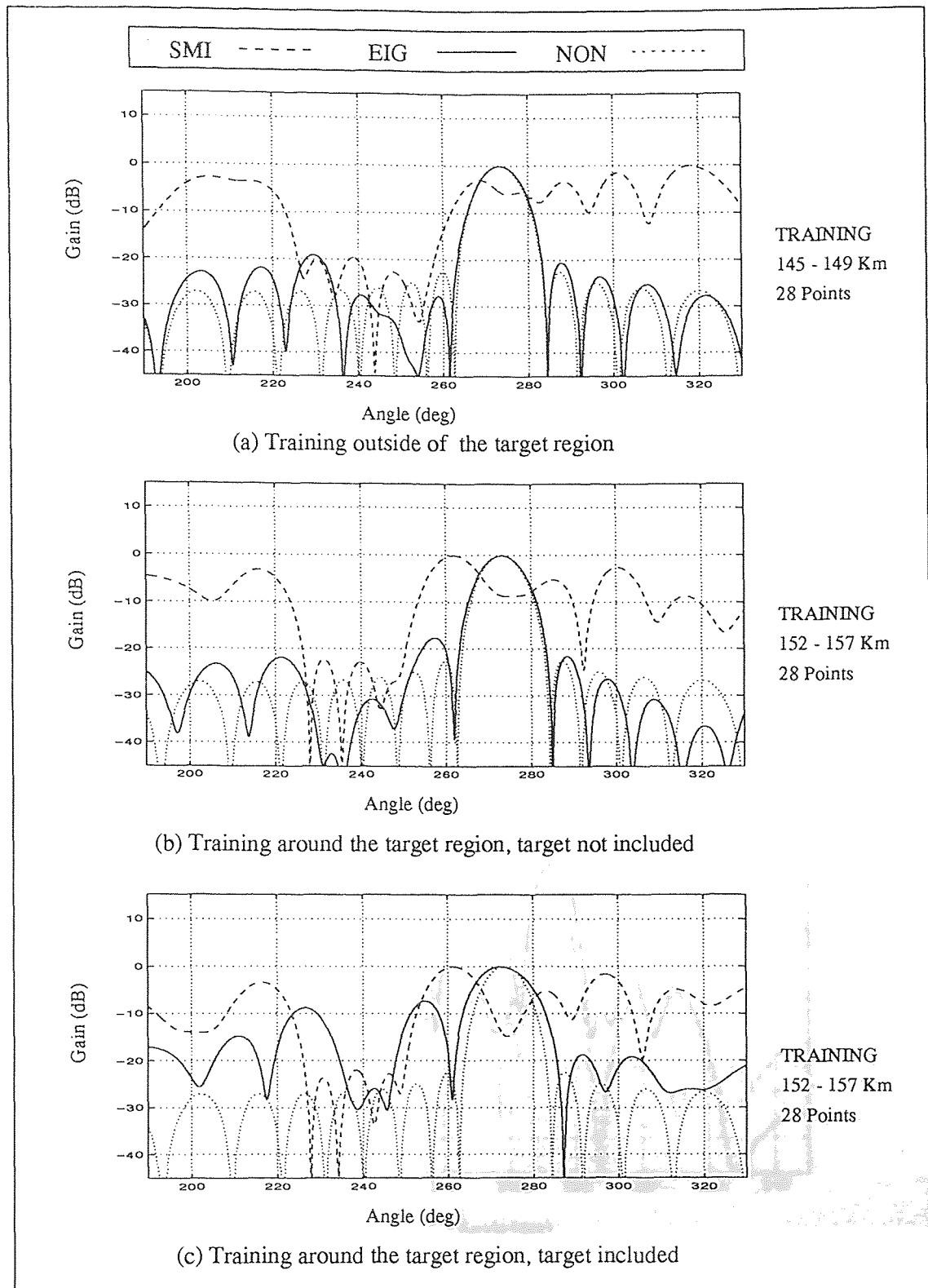


Figure 4.10 Post-Doppler Antenna Pattern Plots Using 28 Training Points

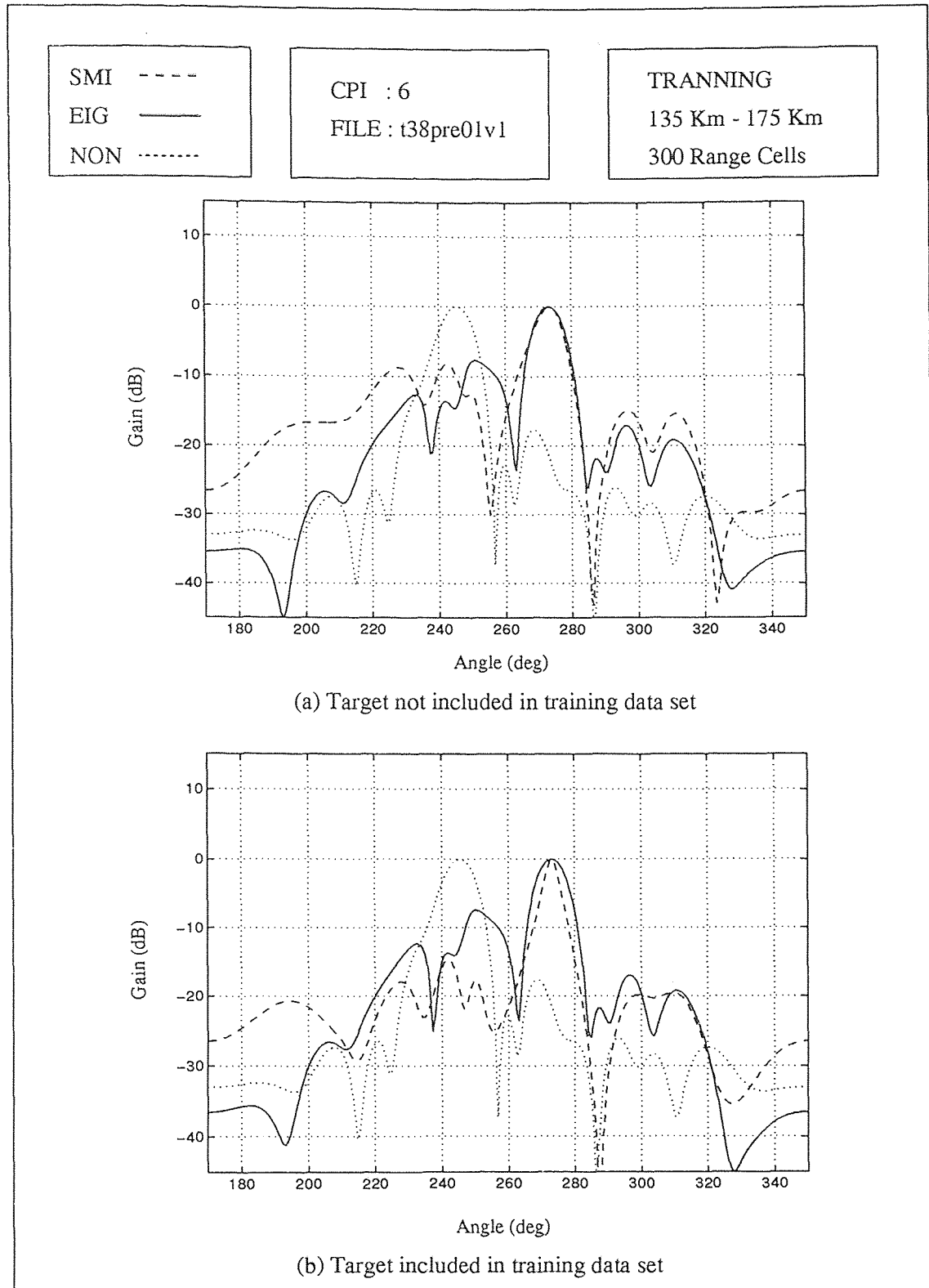


Figure 4.11 Post-Doppler Target Detection Using 300 Training Points

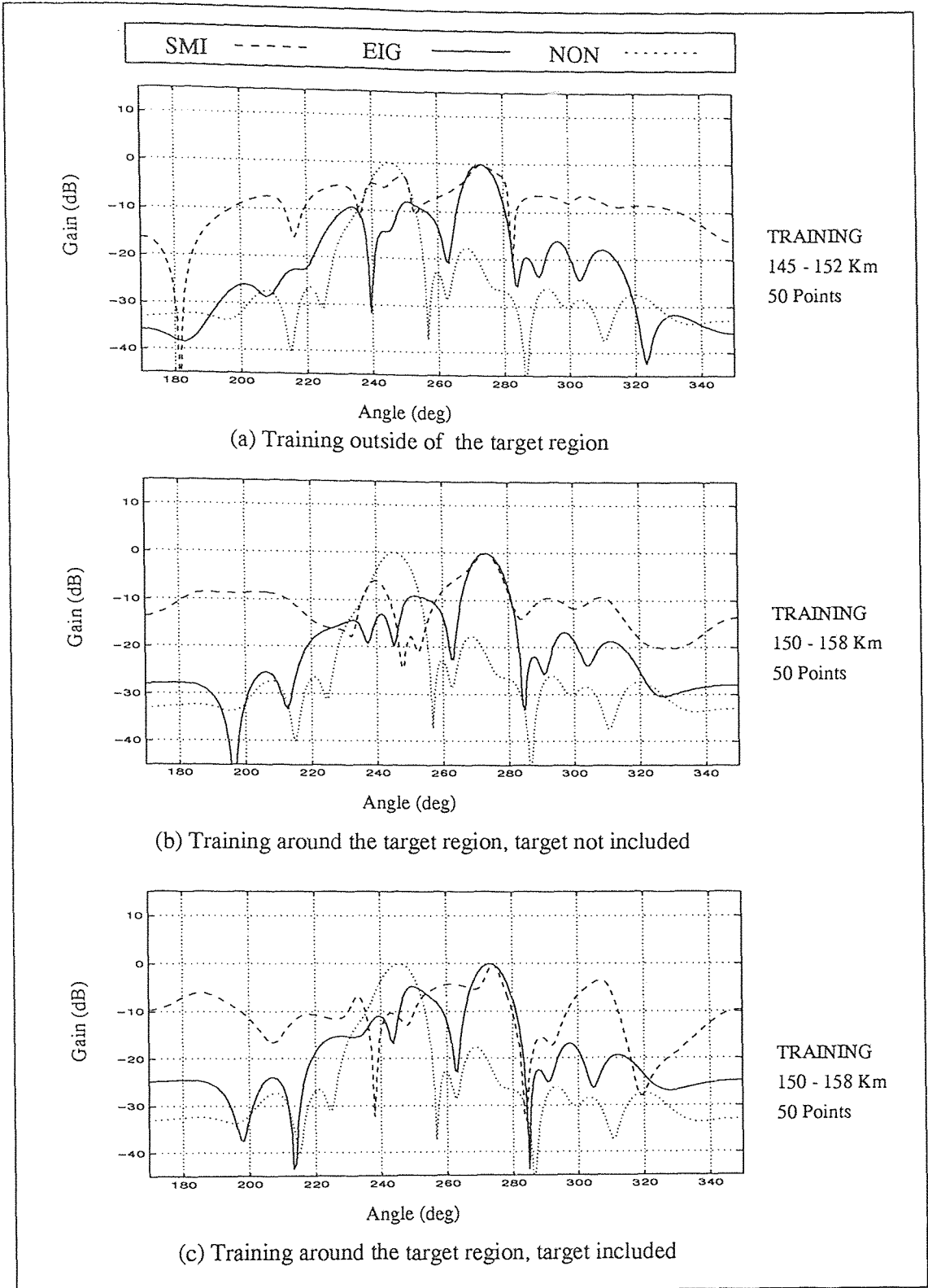


Figure 4.12 Post-Doppler Target Detection Using 50 Training Points

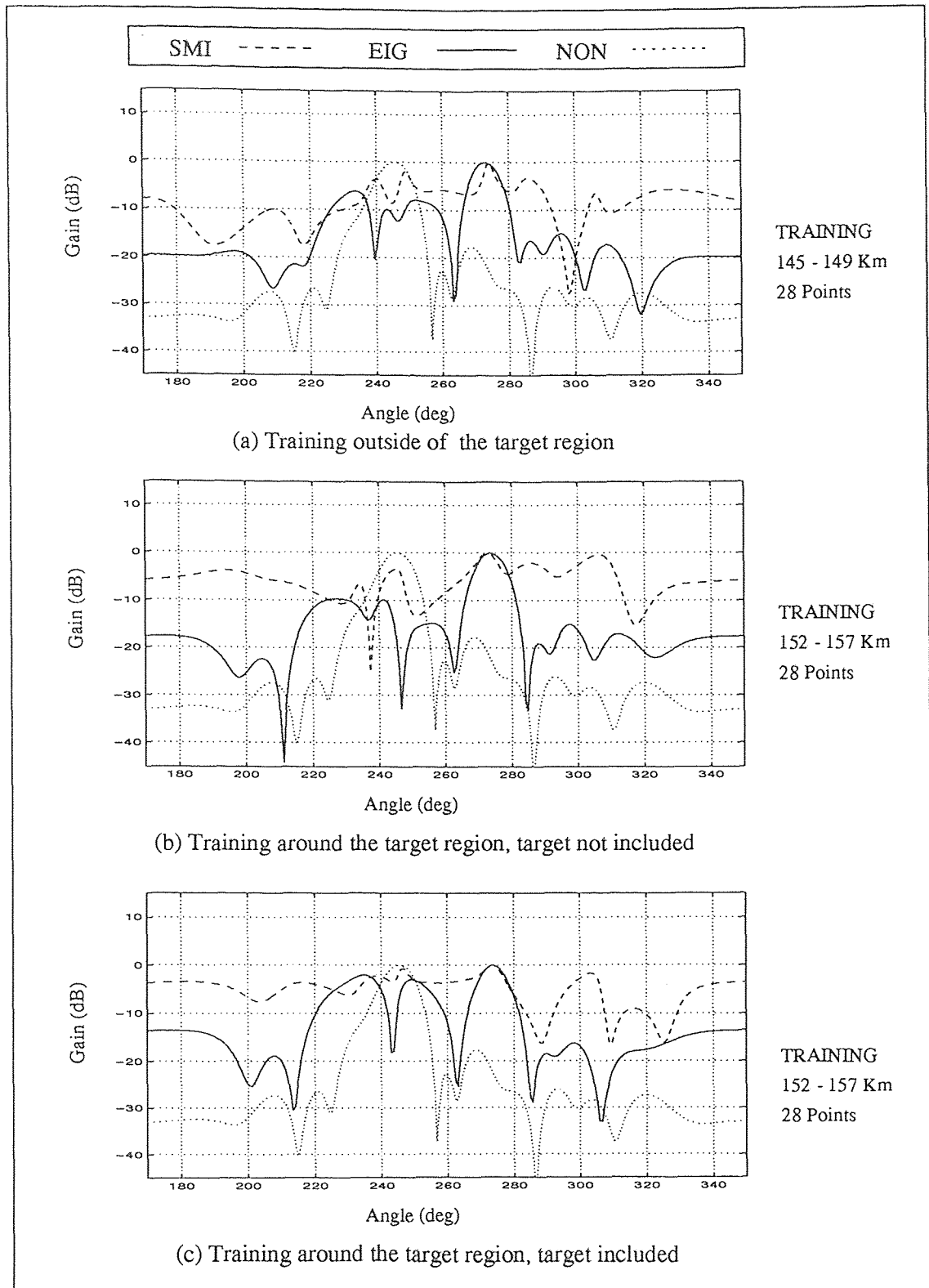


Figure 4.13 Post-Doppler Target Detection Using 28 Training Points

output relative to sky noise, as a function of the number of training points, is plotted. The target region is included in the training set, therefore, when the training support is decreased the desired signal component increases. The eigencanceler performs 4 dB better than SMI when the training set is large. When the training set is decreased, the performance of the SMI is affected more than the eigencanceler's performance is. This plot only provides information about how much the desired signal is preserved, but it does not give any information about how much the interference is cancelled. To study clutter cancellation, the output at the target range is plotted with respect to the background noise at the beamformer's output around the target region. The background noise level is calculated by taking the mean of the beamformer's output from 142 km to 165 km, over 150 points. The target region is not included in the calculations of the mean. Comparing part (a) to part (b), the performance of SMI approaches that of the eigencanceler. This shows that SMI cancels the interference better than the eigencanceler, but the performance is still inferior because of the signal cancellation effect. In Figure 4.14(c), instead of using a fixed region for calculation of the mean as in part (b), the background noise power is calculated using exactly the same region as the training. The performance of the SMI is improved even more because SMI cancels interference in the training region more effectively, but it performs poorly cancelling the interference outside the training region. This was also observed in the range detection plots where a null was placed around the training region, as in Figure 4.5(b). In conclusion, SMI cancels the desired signal as the number of training points is decreased.

The eigencanceler's is a better estimator of global interference than SMI, even with a localized correlation matrix. The eigencanceler uses the eigenvectors that correspond to the largest eigenvalues, which is a better representation of the global interference. On the other hand, SMI uses the inverse of the correlation matrix,

which involves all the eigenvectors. This is a much better estimate locally, but it is not very effective globally.

4.6 Conclusions

In this work, the signal cancellation effects are studied when there is a mismatch between the true desired signal and the presumed theoretical desired signal. Adaptive radar is susceptible to signal cancellation effects when the target signal is included in the training data and in the presence of pointing/calibration errors. It was shown, by analysis and illustrations from the Mountaintop dataset, that the SMI method is very sensitive to the presence of the desired signal component in the estimated correlation matrix, and performance is degraded even with small pointing/calibration errors. The eigenanalysis-based adaptive radar is proven to be much more robust than the SMI method with respect to signal cancellation effects.

The design of calibration filters to minimize the mismatch is explained and the results of the calibration filters are illustrated on the experimental data. Also the pulse compression method to achieve high resolution is explained.

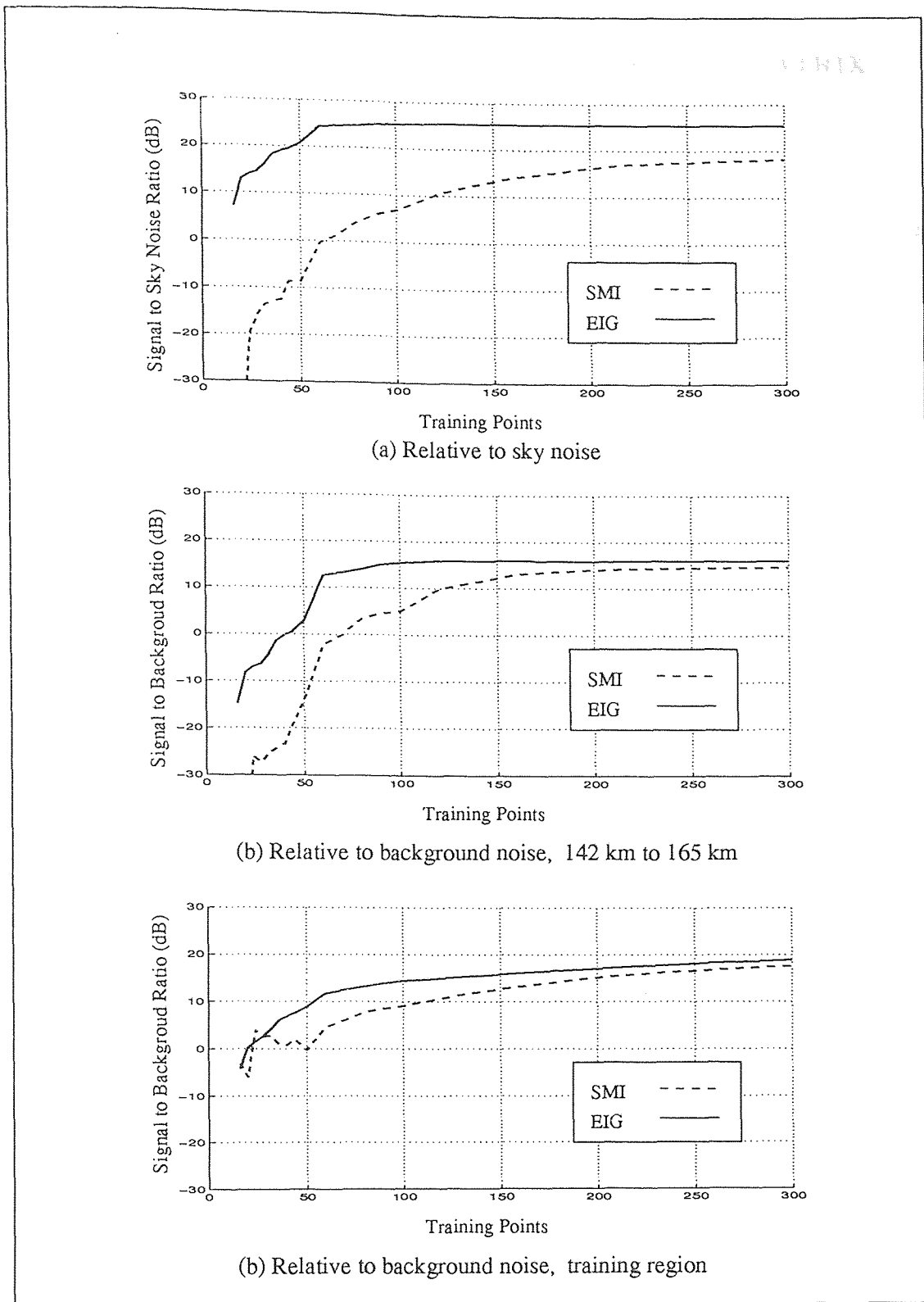


Figure 4.14 Signal Cancellation

APPENDIX A
EIGEN-DECOMPOSITION OF A RANK TWO MATRIX

First consider a rank two $L \times L$ correlation matrix

$$\mathbf{R} = \sigma_d^2 \mathbf{s}_d \mathbf{s}_d^H + \sigma_i^2 \mathbf{s}_i \mathbf{s}_i^H \quad (\text{A.1})$$

\mathbf{R} in terms of its eigen-decomposition is given by

$$\mathbf{R} = \lambda'_1 \mathbf{q}_1 \mathbf{q}_1^H + \lambda'_2 \mathbf{q}_2 \mathbf{q}_2^H, \quad (\text{A.2})$$

where \mathbf{q}_l is the l^{th} eigenvector and λ'_l is the l^{th} eigenvalue. An eigenvector of the correlation matrix expressed as a linear combination of the desired signal and the interference is given by

$$\mathbf{q} = a \mathbf{s}_d + b \mathbf{s}_i. \quad (\text{A.3})$$

The eigenvectors must satisfy the equation

$$\begin{aligned} \mathbf{R} \mathbf{q} &= \lambda' \mathbf{q} \\ (\sigma_d^2 \mathbf{s}_d \mathbf{s}_d^H + \sigma_i^2 \mathbf{s}_i \mathbf{s}_i^H)(a \mathbf{s}_d + b \mathbf{s}_i) &= \lambda'(a \mathbf{s}_d + b \mathbf{s}_i) \\ (a \sigma_d^2 + b \sigma_d^2 \rho_{id}^*) \mathbf{s}_d + (b \sigma_i^2 + a \sigma_i^2 \rho_{id}) \mathbf{s}_i &= a \lambda' \mathbf{s}_d + b \lambda' \mathbf{s}_i, \end{aligned} \quad (\text{A.4})$$

where $\rho_{id} = \mathbf{s}_i^H \mathbf{s}_d$. To satisfy these equations,

$$\begin{aligned} a \sigma_d^2 + b \sigma_d^2 \rho_{id}^* &= a \lambda' \\ b \sigma_i^2 + a \sigma_i^2 \rho_{id} &= b \lambda', \end{aligned} \quad (\text{A.5})$$

and

$$\det \begin{bmatrix} \sigma_d^2 - \lambda' & \sigma_d^2 \rho_{id}^* \\ \sigma_i^2 \rho_{id} & \sigma_i^2 - \lambda' \end{bmatrix} = 0. \quad (\text{A.6})$$

The eigenvalues are obtained by solving equation (A.6),

$$\lambda'_{1,2} = \frac{\sigma_i^2 + \sigma_d^2}{2} \left(1 \pm \sqrt{1 - \frac{4 \sigma_i^2 \sigma_d^2 (1 - |\rho_{id}|^2)}{(\sigma_i^2 + \sigma_d^2)^2}} \right). \quad (\text{A.7})$$

The normalized eigenvectors are obtained from equation (A.5) and equation (A.3)

$$\alpha = \frac{b}{a} = \frac{\lambda' - \sigma_d^2}{\sigma_d^2 \rho_{id}^*} = \frac{\sigma_i^2 \rho_{id}}{\lambda' - \sigma_i^2} \quad (\text{A.8})$$

$$\mathbf{q} = \frac{\mathbf{s}_d + \alpha \mathbf{s}_i}{\sqrt{1 + |\alpha|^2 + 2\text{Re}(\alpha \rho_{id}^*)}} \quad (\text{A.9})$$

Given the solution above, the first two eigenvectors of the correlation matrix

$$\widehat{\mathbf{R}}_x = \sigma_d^2 \mathbf{s}_d \mathbf{s}_d^H + \sigma_i^2 \mathbf{s}_i \mathbf{s}_i^H + \mathbf{I} \quad (\text{A.10})$$

are the same as the \mathbf{R} , since they span the same interference-plus-signal subspace. The first two eigenvalues are $\lambda'_1 + 1$, and $\lambda'_2 + 1$, respectively, due to added noise component. Remaining eigenvectors span the noise subspace with eigenvalues equal to one. This concludes the derivation of equations (3.19) and (3.20).

REFERENCES

1. "Special issue on adaptive antennas," *IEEE Trans. Aerospace and Electronic Systems*, vol. 24 No. 5, Sept. 1976.
2. B. Widrow, "Adaptive arrays-an introduction," *Proc. IEEE*, vol. 55 No. 10, pp. 2143-2159, Dec. 1967.
3. L. J. Griffith, "A simple adaptive algorithm for real-time processing in antenna arrays," *Proc. IEEE*, vol. 57 No. 12, pp. 1696-1704, Oct. 1969.
4. O. L. Frost, III, "An algorithm for linearly constrained adaptive array processing," *Proc. IEEE*, vol. 60 No. 8, pp. 926-935, Aug. 1972.
5. C. L. Zahm, "Applications of adaptive arrays to suppress strong jammers in presence of weak signal," *IEEE Trans. Aerospace and Electronic Systems*, vol. 9, pp. 260-271, 1973.
6. C. L. Compton, Jr., R. J. Huff, W. G. Swarner, and A. A. Ksienski, "Adaptive arrays for communication systems: An overview of research at the Ohio State University," *IEEE Trans. Aerospace and Electronic Systems*, vol. 24 No. 5, pp. 599-606, Sept. 1976.
7. M. H. Er and A. Cantoni, "An alternative formulation for an optimum beamformer with robustness capability," *Proc. Inst. Elec. Eng.*, pp. 447-460, Oct. 1985.
8. F. Habu, Y. Bar-Ness, and C. C. Yeh, "An adaptive interference canceling array utilizing hybrid techniques," *IEEE Trans. Aerospace and Electronic Systems*, vol. 19, Sept. 1983.
9. G. T. Zunic and L. J. Griffiths, "A robust method in adaptive array processing for random phase errors," in *Proceedings Int. Conf. Acoust. Speech Signal Processing*, vol. 24 No. 5, Toronto, Canada, pp. 1357-1360, May 1991.
10. A. M. Vural, "Effects of perturbations on the performance of optimum/adaptive arrays," *IEEE Trans. Aerospace and Electronic Systems*, vol. 15 No. 1, pp. 76-87, Jan. 1979.
11. H. Cox, R. M. Zeskind, and M. M. Owen, "Robust adaptive beamforming," *IEEE Trans. Acoustics, Speech, and Signal Processing*, vol. 35, pp. 1365-1376, Oct. 1987.
12. K. Gerlach, "The effect of I,Q mismatch errors on adaptive cancellation," *IEEE Trans. Aerospace and Electronic Systems*, vol. 28, pp. 729-740, July 1992.
13. H. Cox, "Resolving power and sensitivity to mismatch of optimum array processors," *J. Acoustics Society of America*, vol. 54 No. 1, pp. 771-785, 1973.

14. D. R. Wehner, *High Resolution Radar*, Artech House, Inc., Norwood, MA, 1987.
15. L. E. Brennan and I. Reed, "Theory of adaptive radar," *IEEE Trans. Aerospace and Electronic Systems*, vol. 9, No. 2, pp. 237–252, Mar. 1973.
16. L. E. Brennan, J. Mallett, and I. Reed, "Adaptive arrays in airborne MTI radar," *Trans. Antennas Propag.*, vol. 24, pp. 607–615, Sept. 1976.
17. A. M. Haimovich and Y. Bar-Ness, "An eigenanalysis interference canceler," *IEEE Trans. Signal Processing*, vol. 39 No. 1, pp. 76–84, Jan. 1991.
18. I. P. Kirsteins and D. W. Tufts, "Adaptive detection using low rank approximation to a data matrix," *IEEE Trans. Aerospace and Electronic Systems*, vol. 30, Jan. 1994.
19. D. F. Marshall, "A two step adaptive interference nulling algorithm for use with airborne sensor arrays," in *Proceedings Seventh SP Workshop on Statistical Signal & Array Processing*, Quebec City, Canada, pp. 301–304, June 1994.
20. D. D. Feldman and L. G. Griffiths, "A projection approach for robust adaptive beamforming," *IEEE Trans. Signal Processing*, vol. 42 No. 4, pp. 867–876, Apr. 1994.
21. A. M. Haimovich, "The eigencanceler: Adaptive radar by eigenanalysis methods," *IEEE Trans. Aerospace and Electronic Systems*, 1995. to appear.
22. J. L. Yu and C. C. Yeh, "Generalized eigenspace-based beamformers," *IEEE Trans. Signal Processing*, vol. 11 No. 11, pp. 2453–2461, Nov. 1995.
23. B. Widrow, K. M. Duvall, R. P. Gooch, and W. C. Newman, "Signal cancellation phenomena in adaptive antennas: Causes and cures," *IEEE Trans. Antennas and Propagation*, vol. 30 No. 3, pp. 469–478, May 1982.
24. Y. Bar-Ness, "Steered beam and LMS interference canceler comparison," *IEEE Trans. Aerospace and Electronic Systems*, vol. 19 No. 1, pp. 30–39, Jan. 1983.
25. N. K. Jablon, "Adaptive beamforming with the generalized sidelobe canceler in the presence of array imperfections," *IEEE Trans. Antennas and Propagation*, vol. 34 No. 8, pp. 996–1012, Aug. 1986.
26. H. Wang and L. Cai, "On adaptive spatial-temporal processing for airborne surveillance radar systems," *IEEE Trans. Aerospace and Electronic Systems*, vol. XXX, No. 3, pp. 660–669, July 1994.

27. G. W. Titi, "An overview of the ARPA mountaintop program," in *Proceedings of Adaptive Antenna Systems Symposium*, Long Island, NY, pp. 53-59, Nov. 1994.
28. S. Haykin, *Adaptive Filter Theory*, Prentice-Hall, Inc., Englewood Cliffs, NJ, second ed., 1991.
29. P. Zulch, *Mountain Top Program Summit Data: ASPA 95 Data Distribution*, Rome Laboratory, Griffiss AFB NY 13441, Rome, NY, March 1995.
30. J. R. Klauder et. al., "The theory and design of chirp radars," *Bell System Tech. J.*, vol. XXXIX, No. 4, pp. 745-808, July 1960.
31. I. S. Reed, J. D. Mallett, and L. E. Brennan, "Rapid convergence rate in adaptive radar," *IEEE Trans. Aerospace and Electronic Systems*, vol. 10 No. 6, pp. 853-863, Nov. 1974.